China Instrument and Control Society
Instrumentation
OPEN ACCESS
INSTRUMENTATION, Vol. 13, No. 3, September 2026 https://doi.org/10.15878/j.instr.202600434

Embodied Intelligent Robots

Flexible Sensing for Embodied Robotics: From Materials and Devices to System Integration and Closed-Loop Control

Hongxi Yang[1], Shuai Xian[1], Xin Dong[2], Chengcai Wang[3*], Yong Zhong[1*]

[1] Shien-Ming Wu School of Intelligent Engineering, South China University of Technology, Guangzhou 511442, China

[2] Faculty of Engineering, University of Nottingham, Nottingham NG8 1BB, UK

[3] School of Mechanical Engineering and Automation, Beihang University, Beijing 100191, China

[*] Corresponding author email: zhongyong@scut.edu.cn (Y. Z.) (https://orcid.org/0000-0002-2673-856X), cc_wang@buaa.edu.cn (C. W.) (https://orcid.org/0000-0002-8937-6199)

Abstract: Flexible sensors that bend, stretch, and conform to curved surfaces are being integrated into robotic bodies with increasing frequency, allowing robots to acquire contact, deformation, and near-field environmental information on curved and large-deformation structures. High-sensitivity devices, however, do not automatically produce reliable task-level perception. This review is organized along a traceable evidence chain from observable, transduction, body integration, signal interpretation, and closed-loop control to task outcome, and compares five transduction mechanisms (piezoresistive, capacitive, piezoelectric, triboelectric, and optical) together with material platforms such as liquid metals and hydrogels. It further examines how structural assembly, stretchable interconnects, calibration and drift compensation, multimodal fusion, and feedback control affect system performance. Using dexterous manipulation, deformation and posture estimation, and human-robot interaction as the three task domains, the review separates device metrics, robot-integration demonstrations, and closed-loop task evidence, and applies this evidence grading consistently across all layers. Current work shows that contact tactile sensing has formed a relatively complete real-robot closed loop under limited objects and operating conditions, whereas environmental sensing, cross-platform transfer, and long-term whole-body deployment still lack unified validation. Future priorities should shift from isolated sensitivity improvement toward comparable evaluation under unified conditions, reporting of end-to-end latency and maintenance costs, and perception-decision-action loops with fail-safe fallback.

Keywords: flexible sensing; embodied robotics; multimodal fusion; closed-loop control; robot skin

Copyright: © 2026 by the authors. This article is licensed under a Creative Commons Attribution 4.0 International License (CC BY) license (https://creativecommons.org/licenses/by/4.0/).

Citation: Hongxi Yang, Shuai Xian, Xin Dong, Chengcai Wang, Yong Zhong. "Flexible Sensing for Embodied Robotics: From Materials and Devices to System Integration and Closed-Loop Control." Instrumentation 13, no. 3 (September 2026). https://doi.org/10.15878/j.instr.202600434

1 Introduction

1.1 Scope and Evidence Grading

This review covers the full chain of flexible intelligent sensing for robots: materials and devices, body integration, signal processing and control, and robot applications directly enabled by flexible sensing. General reinforcement learning or control methods, actuators alone, purely medical wearables, and vision-only robotic work are excluded unless their abstracts or full texts explicitly establish a direct connection to flexible sensing in robotics.

The literature was collected from mainstream academic databases and publishers, including IEEE Xplore, ScienceDirect (Elsevier), Wiley Online Library, Nature Portfolio (Springer Nature), Science/AAAS (science. org), ACS Publications, MDPI, and arXiv, with supplementary searches targeting chapter-coverage gaps (search completed in July 2026). Search terms combined sensing targets, transduction mechanisms, and robotic application directions, for example flexible/stretchable sensors, robot skin, tactile grasping, slip detection, soft robot shape sensing, visuo-tactile fusion, and liquid metal/ hydrogel strain sensors, and were adjusted according to identified coverage gaps. The time window focuses on the recent five years (2021-2026), with foundational or classical work extended to before 2015. Inclusion criteria required topical relevance, English language, publication in mainstream journals of the field, and deduplication by DOI, yielding a final set of 97 papers.

The review distinguishes robot-direct evidence from cross-domain device evidence. Robot-direct evidence (validation on a robot body with reported task outcomes) differs from cross-domain device evidence (wearable or medical device results that inform mechanism and material feasibility but cannot be extrapolated to robot performance). Closed-loop control denotes the control behavior; task-level evidence the validation granularity; closed-loop task evidence robot-direct validation with the loop closed. Preprint (arXiv) entries and published papers follow the same verification procedure and are labeled separately. Simulation results support methodological feasibility only and do not constitute task-level evidence. All citations can be traced to verified primary literature, and numerical values and comparisons are based solely on the original sources.

This grading runs throughout the review: each subsection of Chapter 3 reports its current highest evidence level, Table 2 and Table 3 annotate row by row, Chapters 5 and 6 assess the evidence level of cited work, and Chapter 7 uses the grading to summarize the gaps from device to system. The evidence levels used throughout this review are defined in Table 1.

Table 1 Evidence-level definitions

Level	Description
L0	Material or device benchtop testing
L1	Installed on a robot, open-loop demonstration only
L2	Flexible sensing enters closed-loop tasks
L3	Repeated quantitative validation across multiple objects, conditions and trials
L4	Cross-platform, long-term or real-world deployment

Note: Unified evidence-level definitions used throughout this review, serving as the evaluation scale across device, integration, algorithm and application layers; each level is judged by the verified robot installation, open/closed-loop validation, object and condition coverage, and deployment scope in the original papers.

1.2 Background and Positioning of This Review

Robots are evolving from programmed machines dominated by rigid mechanisms toward systems that require stronger physical interaction. Handling fragile objects, adapting to irregular contact surfaces, and working near humans all demand that robots obtain reliable physical information continuously during deformation and contact[1]. Conventional rigid electronics attach poorly to dynamic, irregular surfaces, whereas flexible sensors can bend and stretch, providing the basis for continuous sensing on curved surfaces and compliant components of robots[2]. Device-level performance, however, is not automatically equivalent to robot-level perceptual capability. Verifiable connections still need to be established among materials and devices, body integration, signal interpretation, and control use.

Important parts of this chain have been covered by earlier reviews, but with different emphases. Device-oriented reviews focus on functional materials, novel structures, and machine-learning-assisted intelligent perception of flexible sensors[2], or proceed from transduction mechanisms to intelligent sensing algorithms and wearable applications[3]. System-oriented reviews discuss sensing and feedback in soft robotics through sensors integrated in soft grippers[1], or extend from sensor design to system-level integration and human-interactive applications[4]. These differences in research subjects and organizing scales leave a clear organizing task for a robot-oriented review. Unlike these reviews, the present one is organized not by device category or algorithm family but by the task chain from materials and devices, robot body integration, signal processing, and closed-loop control, and uses one set of verification questions to compare the evidence and limitations of each link in robot tasks.

This review defines flexible intelligent sensing for robots operationally as follows: sensing elements that bend, stretch, or conform are mounted on a robot body to acquire information about the contact interface, body deformation, or the near-field environment, and the readout and signal interpretation produce inputs usable for state estimation, control, or task decisions. Flexibility here refers to the ability of the sensing system to adapt to the deformation of the robot mechanical interface; intelligence refers to the signal being interpretable and entering the task chain, rather than a single device having higher sensitivity. Accordingly, the review uses the traceable chain from materials, devices, body integration, signal processing, control, and task as its main axis of comparison (Fig. 1 summarizes this closed-loop framework and its verification conditions). To keep the framework testable, the same five questions are asked at every layer: what observable the sensing element adds, how it enters the robot stably through mechanical and electrical interfaces, what calibration and interpretation cost the signal incurs, whether control or the task gains

verifiable benefit, and which operating conditions and failure boundaries bound these conclusions. The contribution of this review lies in using this common set of questions to compare the evidence, trade-offs, and maturity of each link, rather than rearranging the catalogue of existing topics.

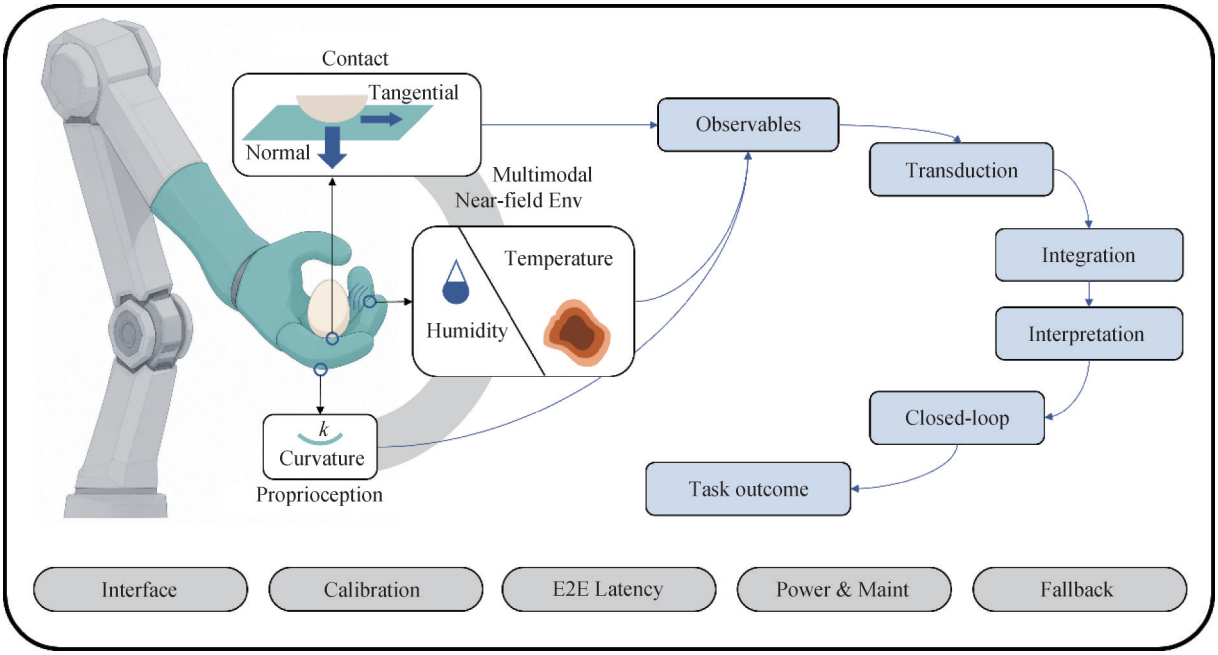


Fig.1 Flexible sensing closed-loop processing chain and system-level validation dimensions. Top: a closed-loop chain from observable, transduction, integration, interpretation and closed-loop control to task outcome, with the outcome fed back to the observation stage; a robotic grasping example indicates three sensing targets (normal/shear contact, body deformation/curvature, and near-field temperature/humidity) and their multimodal relations. Bottom: five system-level validation dimensions used throughout this review: sensor-body interface, full-chain calibration, end-to-end latency, power and maintenance, and fail-safe fallback.

The rest of the review proceeds accordingly. Chapter 2 builds a taxonomy of sensing targets according to where the state resides, distinguishing contact-interface, robot-body, and external-environment information and their multimodal relations. Chapter 3 compares how flexible materials and devices convert this information into readable signals through different transduction mechanisms. Chapter 4 addresses structural integration, conformal and stretchable design, and self-healing and self-powered schemes for moving sensors from device prototypes onto robot bodies. Chapter 5 analyzes how raw signals are converted through correction, representation, learning, and fusion into state estimates and closed-loop control inputs. Chapter 6 evaluates verifiable gains in contact manipulation, self-deformation, and human-robot interaction using robot tasks as the unit of analysis. Chapter 7 summarizes the gaps from device to system and proposes a traceable evaluation path.

2 A Taxonomy of Flexible Sensing for Robots

This chapter classifies flexible intelligent sensing for robots by where the sensed state resides, rather than by device mechanism or material system. The contact interface (Section 2.1) provides local states such as pressure, shear, vibration, slip, and contact thermal properties; the robot body (Section 2.2) provides deformation, posture, and kinematic states; the external environment (Section 2.3) provides non-contact information such as proximity, ambient temperature, and humidity. Two boundaries are worth clarifying because they are easily confused: heat exchange at the moment of contact belongs to tactile sensing, whereas temperature describing the surrounding operating condition belongs to environmental sensing; local contact loads belong to tactile sensing, whereas changes in the overall robot configuration belong to body-state sensing.

Multimodal sensing (Section 2.4) is a relational axis across the three categories above, not a fourth independent source of information. This section discusses only temporal complementarity, spatial complementarity, and physical-quantity coupling; device integration and algorithmic fusion are deferred to Chapters 4 and 5, respectively. With this arrangement, subsequent chapters can answer how signals are generated, how they enter the robot body, and how they are interpreted and used, without mixing levels.

2.1 Tactile Sensing

For a robot, tactile sensing provides local physical information after contact occurs. When the robot end effector contacts an object or the environment, pressure, shear force, slip, vibration, and temperature changes

jointly characterize the interface state [5]; flexible tactile sensing converts these stimuli into interpretable signals [4] to judge whether contact is stable, what surface properties the object has, and whether the action needs adjustment. This section therefore defines tactile sensing as estimation of the contact-interface state, distinguished from body-state sensing and environmental sensing.

The key to classifying tactile sensing is not which device produces the signal but what information the contact interface provides. Normal pressure and its spatial distribution describe contact location and load; tangential force, slip, and vibration describe frictional state and relative motion; contact temperature and the thermal exchange response add the thermal properties of the object. In grasping in particular, separating the normal and tangential components is fundamental to judging contact stability[6], and slip, texture, and contact pressure support action adjustment and object-property inference[7].

The value of tactile sensing for robots lies in providing post-contact states that vision cannot easily obtain. Slip feedback can be used to regulate grip force, and texture, thermal properties, and contact pressure support object-property inference[7]. Together with the robot pose provided by body-state sensing (Section 2.2) and the global geometric cues provided by vision, these interface states form the informational basis of interactive perception. Tactile research has expanded from single-point force to multi-point arrays, multimodal integration, and learning-based recognition, with specific schemes including surface acoustic wave localization[8], tactile-proximity dual-mode sensing[9], triaxial optical tactile sensing[10], and multimodal temperature-pressure coupled sensing[11], as well as machine-learning contact localization on electronic skin[12] and self-powered tactile interaction[13].

2.2 Deformation and Posture Sensing

The essential difference between soft robots and rigid robots is that soft robots achieve motion through the compliant deformation of the structure itself. Conventional articulated robots measure discrete joint angles directly with encoders, whereas soft structures have theoretically continuous distributed degrees of freedom, and their bending, elongation, and torsion vary continuously in space[14]. The task of deformation and posture sensing (body-state sensing) is to acquire in real time the kinematic state of each part of the robot body, providing the perceptual basis for motion control and external-contact judgment.

Deformation and posture sensing first faces an identifiability problem. Local strain, curvature, or cavity state are only directly observable quantities; what the robot actually needs is the overall shape, end-effector posture, and their evolution over time. The mapping from local signals to global states is further affected by heterogeneous interfaces, nonlinearity, and hysteresis[15,16]. More fundamentally, the same bending or elongation can arise from internal actuation or from external contact; without distinguishing the source of deformation, body state cannot be used directly for safe interaction[17].

Accordingly, this section organizes the information needed for body-state sensing into three levels: local strain and curvature describe deformation at each location of the structure, overall shape and posture describe the current robot configuration, and deformation source and contact state indicate whether a change is self-driven or externally imposed. Existing work shows that this information can be obtained from embedded strain, fluidic state, or the difference between desired and actual shape[14,17,18].

Deformation and posture sensing provides the robot with self-state information that tactile sensing (Section 2.1) cannot cover. Tactile sensing captures local pressure, shear, and temperature at the interface after contact; body-state sensing continuously tracks bending angles, end-effector trajectories, and motion states, and is a prerequisite for closed-loop motion control. Comparing desired and actual deformation in real time allows the robot to distinguish its own motion from external contact[17], and this capability constitutes the perceptual basis for safe physical interaction and autonomous environmental exploration.

2.3 Environmental Sensing

Environmental sensing describes physical information that a robot acquires from outside its own body, including proximity before contact and task context such as ambient temperature and humidity. Proximity concerns whether surrounding objects exist, their distance, and the direction of relative motion; environmental physical quantities indicate whether the operating condition can change material, device, or task behavior. In the current literature collection, robot-direct evidence concentrates on proximity and temperature, whereas humidity, gas, and chemical quantities mostly come from cross-domain device studies. This section therefore only defines their informational roles and does not extrapolate non-robotic results to robot performance. Flexible proximity sensing can supplement vision in narrow, occluded, or poorly lit scenarios[19].

Proximity provides near-field spatial information before contact occurs. Existing cases demonstrate proximity arrays with adjustable spatial coverage, stretchable tactile-proximity dual-mode units, and non-contact spatial localization for continuum robots[19-21]. These cases jointly support the information-level conclusion that object presence, distance, and direction can be perceived before contact, but their detection range, resolution, and environmental stability are bounded by each device and test condition, and no route ranking is attempted in this chapter.

Environmental sensing also includes non-contact interaction and environmental physical quantities. A flexible dual-mode skin can distinguish tactile from non-

contact input and use the operator near-field actions as teaching information for a soft robotic arm[22]. A pressure-temperature dual-mode device shows that temperature can be recognized as an environmental variable independent of contact load[23]; however, this result comes from a non-robotic device scenario and supports only the separability of physical quantities, not temperature perception by robots in complex environments. Robot evidence for humidity and other chemical quantities remains insufficient, and their encapsulation, cross-sensitivity, and task use are left as open questions.

Environmental sensing therefore adds external information that tactile and body-state sensing cannot cover: proximity provides near-field object cues before contact, ambient temperature and humidity describe task context, and non-contact interaction conveys human intent. Proximity cannot give contact force, tactile sensing cannot warn before contact, and body-state sensing alone cannot describe the external environment; these boundaries motivate multimodal information synergy (Section 2.4).

2.4 Multimodal Sensing

The preceding sections distinguish the contact interface, robot body, and external environment by where the state resides, yet real tasks often require using this information jointly: proximity provides pre-contact warning, tactile sensing gives the interface state after contact, and body-state sensing tracks the robot configuration, with each modality having its own blind spots. Multimodal synergy is therefore a relational layer over these three categories, and the emphasis is on which information is complementary, which physical quantities are coupled, and how these relations change task decisions, rather than simply increasing the number of sensors.

Existing cases support three types of relations. Temporal complementarity appears when proximity provides warning before contact, tactile sensing confirms the interface state after contact, and body-state sensing continuously tracks the robot configuration[22]. Spatial complementarity appears when the near-field space, contact interface, and overall deformation are covered by proximity, tactile, and body-state sensing, respectively[19]. Physical-quantity coupling requires clarifying the informational role of each modality before separating or fusing quantities such as pressure and temperature that change simultaneously[23]. These evidence items support synergy in the corresponding tasks only; multimodality itself should not be treated as an independent sensing target, and adding channels should not be assumed to improve performance regardless of task.

3 Flexible Sensing Materials and Devices

Chapter 2 defined the information a robot needs according to sensing targets; this chapter examines how flexible materials and devices convert this information into readable signals. The classification is organized primarily by transduction mechanism (Fig. 2 illustrates the signal-generation principle of five mechanisms), comparing piezoresistive (Section 3.1), capacitive

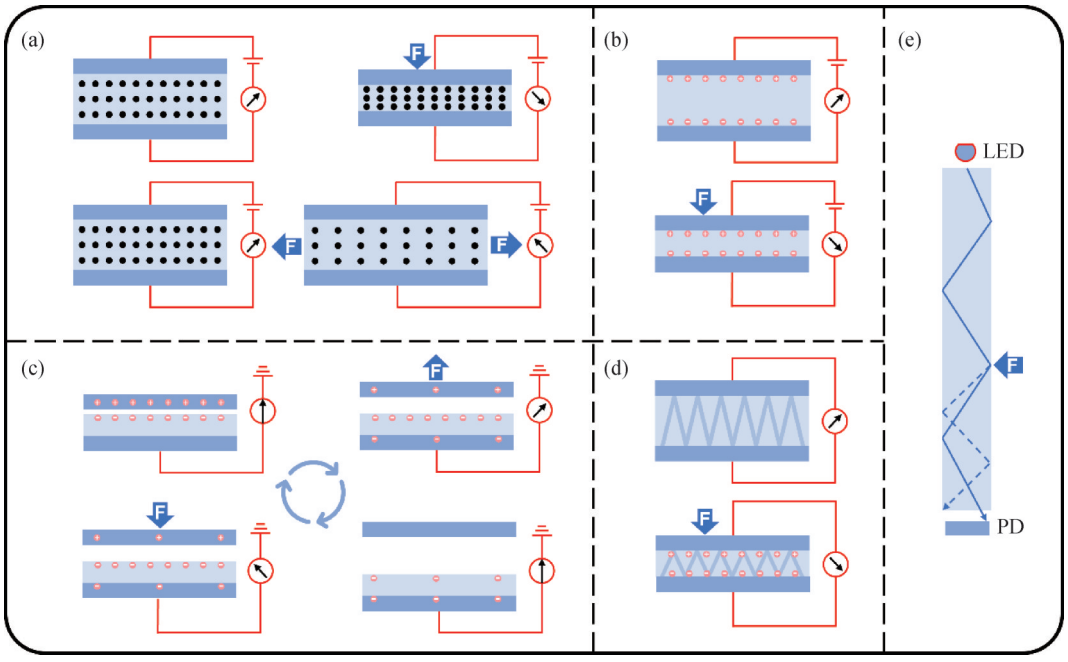


Fig.2 Five major transduction mechanisms of robot flexible sensing. (a) Piezoresistive: external force alters the contact state of conductive fillers in an elastomeric matrix, changing resistance. (b) Capacitive: changes in electrode distance, overlapping area or dielectric constant vary capacitance. (c) Piezoelectric: dynamic stress induces polarization charge in piezoelectric materials. (d) Triboelectric: coupling of contact electrification and electrostatic induction generates electrical signals. (e) Optical: LED-photodiode (PD) pairs sense elastomer deformation through modulation of optical path, intensity or wavelength.

(Section 3.2), piezoelectric and triboelectric (Section 3.3), and optical (Section 3.4) sensing in turn. Liquid metals and hydrogels, which serve as material platforms for multiple transduction mechanisms, are treated separately in Section 3.5.

To avoid conflating mechanisms with materials, each section follows four steps: what can be measured, under which conditions the approach is advantageous, what problems arise when integrated into a robot, and the current highest evidence level; structures, performance, and applicable boundaries are then compared. Table 2 groups representative devices from Sections 3.1-3.5 with condition-bound metrics, robot evidence levels, and deployment bottlenecks. This two-dimensional organization preserves the existing chapter order while providing explicit device-level input for the discussion of

Table 2 Condition-bound evidence comparison of flexible sensing mechanisms and material platforms

Mechanism/ platform	Measurand	Condition-bound metrics	Robot evidence	Deployment bottleneck	Evidence level	Reference
Piezoresistive	Pressure	3656.8 kPa^{-1} (0-100 kPa), range up to 3000 kPa	Array + deep learning (wearable)	Temperature/humidity drift, cyclic fatigue, cross-device consistency	L0	[24]
Piezoresistive	Pressure	Sensitivity 7.66 kPa^{-1}, R^2 =0.99 (0-583 kPa)	Finger-press/wearable demo	Microstructure fatigue, viscoelastic hysteresis	L0	[26]
Piezoresistive	Pressure (grid textile)	Sensitivity 934.6 kPa^{-1} (0-390 kPa)	Fabric array + SVM (automotive HMI)	Cross-device generalization unverified, interconnection calibration	L0	[32]
Capacitive	Pressure	Sensitivity 33.7 kPa^{-1} (0-1700 kPa), detection limit 0.36 Pa	Robotic hand demo	Hydration stability, temperature drift, hysteresis	L1	[34]
Capacitive	Triaxial force	Normal 0-46 N, shear 0-10 N; 240 channels, 11 ms	UR10 + gripper grasp feedback (open loop)	EMI shielding, interconnection and array calibration	L1	[37]
Capacitive	Normal & shear distribution	Wireless fabric array; three EMI shielding schemes	Parallel-gripper force-mapping grasp	Shielding trade-off, bandwidth and multi-channel readout	L1	[38]
Piezoelectric/ Triboelectric	Tactile (TENG)	0.308 $V \cdot kPa^{-1}$, linearity 0.99, $>10^4$ cycles	Soft-gripper posture classification ≈96%	Humidity sensitivity, high output impedance; self-powered ≠ system power	L1	[46]
Piezoelectric/ Triboelectric	Dynamic + static strain	PVDF/MWCNT piezoelectric-piezoresistive dual-channel fusion	No robot installation	Static attenuation requires a supplementary channel	L0	[48]
Optical	Triaxial force + slip	Normal 2.88 V/N, 22 ms, overload >450 N	Dexterous-hand slip-compensated grasping	Light-source/packaging volume; latency depends on readout	L2	[50]
Liquid-metal platform	Pressure + deformation	Liquid-metal sprayed silicone skin (distributed)	Robot-hand softness identification	Oxide-layer interface changes, leakage, packaging dependence	L1	[56]
Hydrogel platform	Strain + tactile	LSTM recognition 98.64% (25 °C, 10 classes), among three condition sets	Three-finger soft gripper force control + recognition	Dehydration, temperature sensitivity, baseline drift	L2	[59]
Self-healing material	Piezoresistive strain + temperature + TENG	Fully intrinsic self-healing, no external healing agent	Conformal soft-robot integration (posture/ material)	Three-function cooperative recovery under cyclic robot loading unverified	L1	[60]

Note: Each row reflects independent test conditions (materials, structures, ranges and metric definitions differ); rows are not directly comparable for ranking. Evidence levels follow Table 1: L0 = benchtop device testing; L1 = installed on a robot, open-loop demonstration only; L2 = flexible sensing enters closed-loop tasks; L3 = repeated quantitative validation across multiple objects, conditions and trials; L4 = cross-platform, long-term or real-world deployment. Abbreviations: TENG = triboelectric nanogenerator; EMI = electromagnetic interference; SVM = support vector machine; HMI = human-machine interface; PVDF = polyvinylidene fluoride; MWCNT = multi-walled carbon nanotube; LSTM = long short-term memory.

mechanical interfaces, electrical interconnects, and encapsulation in Chapter 4.

3.1 Piezoresistive Sensors

Flexible piezoresistive sensors measure pressure or strain through resistance changes caused by external force; the physical basis is that force alters the contact state of conductive fillers in an elastomeric matrix and reconfigures the conductive pathways. Performance is jointly determined by the conductive material, microstructure, and substrate. High sensitivity, wide linear range, and large measuring range do not hold simultaneously in all structures, and the specific trade-off is further constrained by loading range, frequency, and material viscoelasticity.

When carbon-based percolation networks are combined with microstructure engineering, piezoresistive devices can achieve both relatively high sensitivity and good linearity within a given range. A multiwalled carbon nanotube (MWCNT)-sprayed hook-and-loop fabric fiber reports a sensitivity of 3656.8 kPa^{-1} over 0-100 kPa, with the detection range extendable to 3000 kPa, and has been built into a 16 × 16 pixel array[24]. A chitosan-fiber MXene point-line conductive architecture maintains 1.16 kPa^{-1} over a 1.5 MPa linear range and reaches 98.61% classification accuracy for six human actions using a convolutional neural network (CNN) [25]. Multilayer hemispherical microstructures achieve a sensitivity of 7.66 kPa^{-1} with linearity of $R^2 = 0.99$ over 0-583 kPa[26], and photocrosslinked strain-localizing microcage structures reduce deformation spillover between adjacent pixels by 90.3%[27]. Geometric design only shifts the local working range; the final trade-off is still governed by structural dimensions, material fatigue, and loading conditions, and is not guaranteed by microstructuring per se. Carbon-based systems can also carry multiphysical sensing: a fully printed MWCNT-graphene oxide device with a low temperature coefficient of resistance of 0.182% per degree Celsius provides pressure-humidity dual-mode output[28], although cross-sensitivity to temperature and humidity, cyclic drift, and cross-device consistency still need evaluation under operating conditions. These results correspond to different structures, ranges, and tasks and cannot be ranked directly by sensitivity values.

Fabric- and fiber-based routes offer breathability, compliance, and compatibility with large-area fabrication for robot-wearable integration, and can be embedded in flexible skins by weaving, embroidery, or sewing. Computerized flat knitting supports layout customization in robot skins[29]; all-fabric hierarchical structures and embroidered core-sheath yarns provide tuning room for sensitivity, range, and response time[30,31]; and grid textiles achieve 934.6 kPa^{-1} sensitivity over 0-390 kPa through alternating MXene/PEDOT: PSS spraying, with the fabric-array signals fed to a support vector machine (SVM) for classification[32]. These numbers correspond to different physical quantities, device areas, test ranges, loading conditions, and metric definitions, so the fabric route cannot be ranked horizontally against thin-film routes on this basis. For robot deployment, the main open issues of the fabric route remain cyclic lifetime, washing and abrasion tolerance, and calibration consistency after large-area interconnection.

The main boundaries of the piezoresistive route come from microstructure fatigue, viscoelasticity of the elastomeric matrix, and baseline shifts caused by ambient temperature and humidity; repeated robot gripping amplifies these effects. Evaluation therefore should not rely on initial sensitivity alone but should also report loading frequency, post-cycle drift, and recalibration cost. Current piezoresistive cases are mostly at evidence level L0: most remain human-wearable or benchtop demonstrations. Robot-body integration demonstrations, such as computerized flat-knitted robot skins, are still mainly open-loop, and no work has entered closed-loop tasks. Compared with capacitive sensors, piezoresistive schemes are structurally simpler with broader material choice, but same-condition comparison of sensitivity, linearity, range, and power is still lacking.

3.2 Capacitive Sensors

Flexible capacitive sensors perceive force and strain through changes in electrode spacing, overlapping area, or dielectric constant, with the ideal relation $C = \varepsilon A/d$. In the ideal static case no continuous conductive current is needed, but actual power consumption, hysteresis, temperature drift, and long-term stability depend on the viscoelasticity and hydration state of the dielectric layer, parasitic capacitance, strain crosstalk, and readout circuitry. The core engineering problem is balancing sensitivity, linearity, and immunity to interference for a given structure and operating condition.

Under specific conditions where microstructured dielectric layers are combined with iontronic interfaces, capacitive responses can be markedly enhanced. An ionogel-microcolumn electrode combination reports 33.16 kPa^{-1} sensitivity over 12-176 kPa and completes a prosthetic-hand grasping demonstration[33]. A gradient micro-pyramid iontronic sensor maintains 33.7 kPa^{-1} sensitivity over 0-1700 kPa with a detection limit of 0.36 Pa, used in an interactive robotic hand[34]. Ionic capacitance combined with hierarchical microstructures retains 98% of pressure sensitivity under 50% tensile strain with a 0.2 Pa detection limit, and has verified quantitative pressure sensing on a soft robot skin[35]. Iontronic interfaces improve response only for specific structures and pressure ranges; linear range, hydration stability, hysteresis, and long-term drift still depend on material state and readout conditions. Multiaxial perception arises from specific electrode layouts, structural decoupling, and calibration models: an asymmetric microhair array distinguishes static and dynamic shear directions over 30 Pa-300 kPa and

survives 5000 cycles[36]; a triaxial capacitive array reads 0-46 N normal force and 0-10 N tangential force in 11 ms through a 240-channel acquisition system[37]. Multiaxial capability therefore cannot be claimed as an inherent advantage of the capacitive route.

Whether capacitive arrays scale to robot systems depends on whether shielding, interconnection, addressing, and calibration can be codesigned with the device. A wireless fabric array compares three shielding schemes and detects normal- and shear-force distributions in grasping experiments[38]. A rigid-island stretchable-interconnect array classifies elastic moduli of materials over 72 kPa-1.36 MPa on a dynamic gripper[39]. UV laser patterning enables in-situ integration of microporous dielectric layers with flexible circuits[40]. Edge computing can absorb part of the readout cost: in-memory analog multiply-accumulate completes noise suppression and edge detection, with single sensing-computing operations consuming more than 22x less power than conventional digital-analog hybrid systems[41]. A multilayer capacitive pad (100 × 100 mm) detects five touch points simultaneously and estimates contact force, but each device still requires a separately trained calibration model[42]. Transparent fingerprint arrays and wearable multi-channel detection also belong to this route[43]. Scalability is therefore determined not only by pixel count but also by spatial calibration, readout bandwidth, computation location, and cross-device consistency.

The main boundaries of capacitive sensing include parasitic capacitance and environmental electromagnetic interference drowning weak signals, electrode area-spacing coupling under stretching, and multichannel bandwidth and power constraints of large-area arrays. In robot applications, electromagnetic shielding, strain isolation, and array addressing jointly determine whether device performance becomes stable system signals. Current capacitive evidence levels are L0-L1: in-memory computing and transparent arrays are device-level work at L0[41,43]; grasping and classification demonstrations installed on prostheses, robot hands, or grippers are L1[33,34,36-39,42]; no case has entered force-control or slip closed-loop tasks. Hysteresis, temperature drift, and linearity cannot be generalized apart from the dielectric layer and operating conditions.

3.3 Piezoelectric and Triboelectric Sensors

Piezoelectric and triboelectric sensors both convert mechanical action into electrical signals, but self-powered sensing means only that the transduction stage does not require external bias; it does not mean the whole node can power itself. The direct piezoelectric effect relates stress or strain to polarization charge; actual current output depends on the rate of change and the readout circuit, and the voltage is also affected by device capacitance, leakage, and time constant, so piezoelectric sensing is usually better suited to dynamic or changing signals. Triboelectric sensors rely on contact electrification and electrostatic induction, and their output is jointly affected by the displacement and velocity of contact, separation, or sliding.

The applicable conditions of triboelectric schemes are tied to material pairing and structural mode. Strongly electronegative materials such as PTFE, FEP, and PDMS act as charge acceptors, polyamide as a charge donor, and liquid metals, being conductive and stretchable, can also serve as TENG electrodes. Vertical contact-separation, horizontal sliding, and single-electrode modes correspond to normal contact, shear detection, and simplified wiring, respectively. An asymmetric-structure TENG outputs two independent signals for parallel pressure and temperature sensing and maintains 94% object-recognition accuracy at operating temperatures up to 200 degrees Celsius[44]. The combination of liquid-metal-silicone composites with embedded 3D printing enables conformal integration of TENGs with soft robot bodies. One-step printing of silicone/CNT composite electrodes and silicone triboelectric layers can produce planar arrays and complex three-dimensional structures such as gyroid networks[45]. A liquid-metal-silicone self-encapsulating conductive ink developed through catalyst diffusion further allows sensors and soft actuators to be fabricated in a single process. The resulting TENG tactile sensor shows 0.308 V/kPa sensitivity, linearity of about 0.99, and durability over 10,000 cycles; embedded in a soft gripper, it reaches about 96% posture-classification accuracy with a CNN[46]. Together these results demonstrate a full-chain fabrication capability from material ink to sensor-actuator integration.

For the piezoelectric route in flexible sensing, the material choice is dominated by PVDF and its copolymer P(VDF-TrFE), whose flexibility, low acoustic impedance, and film-forming ability suit conformal devices; its piezoelectric coefficient is lower than that of some inorganic ceramics, but the mechanical match is more favorable for flexible integration[47]. Composite films can use a piezoelectric channel for dynamic strain and a piezoresistive channel for static strain and fuse the two signals[48], showing that static information can be supplied by a combined mechanism or an additional channel.

When integrated into robots, charge leakage and readout time constants attenuate signals under constant deformation, so steady-state or quasi-static measurement usually needs supplementary channels such as piezoresistive or capacitive ones. This is a working boundary, not a law of physics that renders the device unresponsive. Triboelectric schemes are sensitive to humidity, surface state, and contact history, and their high output impedance raises front-end readout requirements. Robot deployment also requires handling operating frequency bands, moisture-proof encapsulation, and signal conditioning. The self-powered property of TENGs reduces bias requirements at the transduction stage but

not the system-level energy budget (Section 7.3). Current evidence levels for piezoelectric and triboelectric sensing are L0-L1: 3D-printed fabrication is device-level validation (L0)[45]; robot-hand recognition[44] and gripper posture classification[46] are open-loop (L1); no work has entered closed-loop tasks. Reference[47] is a review-level overview and does not participate in the evidence chain. Optical, liquid-metal, and hydrogel platforms are compared in Sections 3.4 and 3.5, respectively.

3.4 Optical Sensors

Flexible optical sensors modulate optical path, intensity, or wavelength through elastomer deformation, and can be divided into three routes: intensity modulation, fiber Bragg grating (FBG) wavelength shift, and vision-based imaging. Optical readout is not directly affected by electromagnetic pickup at the sensing end and provides electrical isolation; however, the system still requires light sources (e. g., LEDs or laser diodes) and photodetectors for intensity-modulation readout, cameras for vision-based imaging, or optical fibers with wavelength-demodulation equipment for FBG readout, so size, power consumption, bending loss, and temperature compensation must enter the integration evaluation. Strain sensing through traditional FBGs cannot distinguish strain caused by twist from strain caused by bending, and intrinsic twist induced during fiber integration calls for manual calibration[49].

Where electromagnetic immunity or electrical isolation matters, the advantage of the optical route holds for specific readout architectures. A soft triaxial optical force sensor based on an LED-photodiode pair measures elastomer deformation and reports a normal-force sensitivity of 2.88 V/N, a 22 ms response, and overload capability beyond 450 N, combined with a gated recurrent unit (GRU) for grip-force monitoring, slip detection, and adaptive grasping[50]. The vision-based route estimates triaxial force through marker tracking and deep learning, with a minimum mean squared error of 0.15 N, and verifies adaptive force grasping on a mechanical gripper at a 30 Hz update rate[51]. These two works show that the optical route has robot-task potential, but cost, encapsulation, and real-time performance still depend on the specific readout architecture.

Integrating optical schemes into robots faces three types of interface challenges: intensity modulation requires a stable light source and optical alignment, FBG requires wavelength-demodulation equipment, and vision-based imaging requires cameras and image-processing compute. The FBG route discussed here concerns single-core fiber gratings, for which bending loss is an inherent concern: it is significant at small bending radii and degrades the sensing signal once the cumulative loss exceeds a threshold[52], and a single core cannot resolve bending direction or separate twist-induced strain; multicore FBG fibers, by separating sensing cores, can resolve bending direction and twist and are therefore preferred in robot shape sensing[49, 53]. Temperature compensation and the size and power of light sources, detectors, and cameras remain unavoidable in every route.

The current highest evidence level of the optical route is L2: the soft triaxial optical force sensor of Mo et al. triggers force increase through tangential-force feedback on a dexterous hand and compensates slip, forming a sensing-control closed loop[50], making it one of the few routes in Chapter 3 that reaches closed-loop validation. That demonstration, however, does not report repeated success rates or end-to-end closed-loop latency, and thus does not meet the L3 requirement of repeated quantitative validation over multiple objects.

3.5 Liquid-Metal and Hydrogel Material Platforms

Liquid metals and hydrogels are not transduction mechanisms but conductive, dielectric, or ionic-conductive media that can serve piezoresistive, capacitive, and triboelectric mechanisms. This section explains, by material platform, the deformation-adaptation capability they provide and the boundaries of encapsulation, interfaces, and long-term stability, without repeating device details already covered under each mechanism.

Typical liquid-metal systems include eutectic gallium-indium and gallium-indium-tin alloys. Room-temperature fluidity and relatively high conductivity (about 3.4×10^{6} S/m[54]) allow them to serve as microfluidic piezoresistive channels, stretchable capacitive electrodes, or triboelectric functional layers. Patterning routes such as injection, direct writing, spraying, templating, and selective wetting each involve trade-offs in resolution, interfacial adhesion, and scalability[55]. In robotic scenarios, liquid metal sprayed on a silicone substrate can build a distributed pressure- and strain-sensing skin that identifies contact position and object softness from compression and lateral-deformation signals[56]; printable liquid-metal conductive inks[57] and polyphenol-induced adhesive metal inks[58] further extend fabrication and interfacial-control options. Engineering boundaries include interface changes caused by the oxide layer, short-circuit risk from leakage, and dependence on encapsulation integrity.

Ionic-conductive hydrogels sense pressure and strain through deformation-induced changes in impedance or capacitance, and their high water content, low modulus, and stretchability favor matching with soft structures. An antifreeze ionic hydrogel integrated into a three-finger soft gripper achieves LSTM recognition accuracies of 98.64% for ten object classes at 25 degrees Celsius, 99.0% for five classes at -20 degrees Celsius, and 90.58% for four classes under four orientations, and demonstrates force-controlled grasping and slip compensation[59]. The three result sets correspond to different object counts and conditions and cannot be merged into a general performance figure. Long-term stability of hydrogels is

jointly affected by hydration state, ion mobility, temperature, and cyclic loading; evaluation should report encapsulation and water retention, ion-electronic interface stability, electromechanical coupling fatigue, and recalibration requirements together.

In terms of evidence levels, the robot evidence for the liquid-metal route is L1: the sprayed silicone skin is an open-loop identification integrated on a robot[56], and references[54] and [55] are review-level overviews. The hydrogel route reaches L2: PID force control and slip compensation form a closed loop[59], but multi-object recognition and single-object closed-loop tuning do not satisfy the L3 requirement of repeated quantitative validation.

4 Integration of Flexible Sensors with the Robot Body

Chapter 3 discussed how flexible sensors generate signals through different transduction mechanisms. This chapter addresses the next critical link: integrating sensors from device prototypes onto the robot body (Fig. 3 summarizes the overall workflow from body integration, through the signal chain, to control loops, together with the system budget). The core tension is that sensors need flexibility and stretchability to attach to curved robot surfaces, while simultaneously requiring reliable mechanical fixation, electrical connection, and environmental protection to guarantee signal quality. The gap between device performance and system-level perception quality is largely determined by engineering choices at the integration stage. The chapter proceeds on three levels: structural integration strategies (Section 4.1) address the engineering of physical mounting, interconnection, encapsulation, and array readout; conformal and stretchable integration (Section 4.2) addresses strain coordination between sensor and body under the large deformations produced by robot motion; and self-healing and self-powered integration (Section 4.3) addresses the long-term usability of integrated systems under damage recovery and energy constraints.

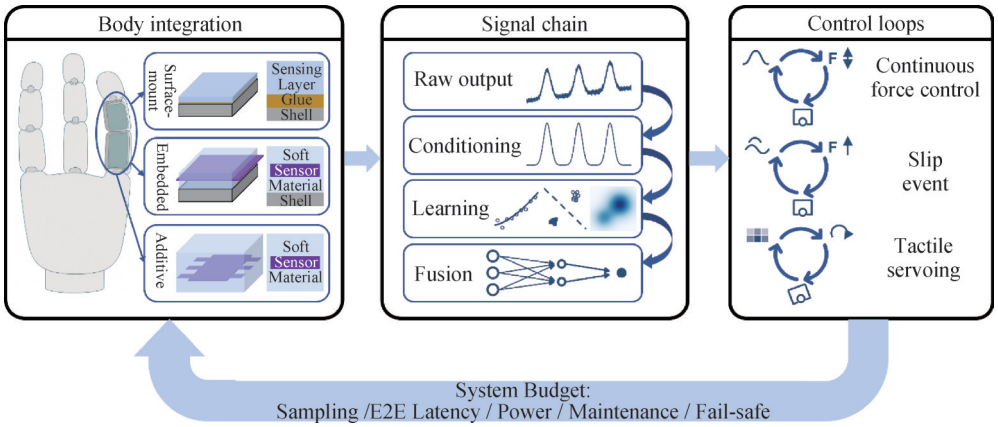


Fig.3 Cross-chapter system workflow from devices to closed loops. Left column: three integration routes of sensors with the robot body—surface attachment, embedded molding and additive manufacturing. Middle column: signal chain from raw output, signal conditioning and learning-based recognition to multimodal fusion. Right column: three control loops—continuous force control, slip-event triggering and tactile servoing. Bottom bar: system budget constraints of sampling, end-to-end latency, power, maintenance and fail-safe behavior, jointly determining the traceability from device metrics to task gains.

4.1 Structural Integration Strategies

Mechanical mounting first determines whether a sensor can conform to the body and remain maintainable. Surface attachment is convenient for replacement, but long-term adhesion, conformal contact on curved surfaces, and contamination protection need separate verification. Embedded molding improves protection but increases repair difficulty; for example, Chen et al. embed sensing elements directly inside a soft actuator for integrated sensing[61]. 3D-printed integration places body structure and sensing function in the same fabrication process, reducing assembly steps. The GenTact-Prox system of Kohlbrenner et al. covers a robot body with modular 3D-printed units and verifies collision avoidance on a Franka arm[62]; Yang et al. build a whole-body-scale skin from distributed modules and multilayer fabrics[63]. These two cases illustrate a system-level trade-off between modular maintainability and continuous coverage, and mounting schemes cannot be chosen by device softness alone.

From the flexible sensing layer to rigid acquisition, computation, and power units, soft-rigid interfaces and strain-relief paths must also be designed. Neutral-plane serpentine interconnects and rigid-island flexible-bridge interfaces have device-level validation[39,63]; interface selection depends on connection pitch, bending radius, repairability, thermal management, and cyclic loading. Encapsulation is an independent link beyond mechanical fixation and interconnection: while providing environmental protection, it must not alter the stress transfer and response of the sensor through mismatches in modulus, thickness, or thermal expansion. The review of

Pyo et al. points out that moisture, sweat, and water permeation are major causes of long-term performance degradation, and that encapsulation technology should be designed together with the system[4]. In the capacitive array of Berman et al., the unloaded baseline still drifts upward by 6.5% after 3000 force cycles[39]; even when device-level tests pass, drift and recalibration costs must enter the acceptance criteria.

Array readout requires choosing among spatial resolution, refresh rate, crosstalk, wiring count, and system cost. Cross-electrode addressing reduces leads but introduces parasitic crosstalk; time-division multiplexing trades refresh rate for circuit simplification; and active matrices improve data fidelity with pixel-level switching at the cost of increased flexible-fabrication and encapsulation complexity[64]. Johnson et al. report a daisy-chained SPI bus architecture for a large-area fabric piezoresistive array, showing that bus topology itself is a design variable in scaling multi-unit readout[65]. Yang et al. use sparse sensing elements combined with super-resolution and tomographic reconstruction to raise perceptual resolution[63], representing another route that trades algorithm for partial hardware density. The final system cost also includes analog-to-digital conversion, cabling and connectors, clock synchronization, heat dissipation, calibration, and maintenance, far beyond the number of sensing elements.

Readout architecture solves how signals are acquired; spatial calibration solves where the signals are. For sensing arrays mounted on complex curved surfaces, the actual positions of individual elements in the robot coordinate frame deviate from design values, and these deviations amplify progressively in kinematic calculations and control outputs. Moussaoui et al. propose a B-spline-surface spatial calibration method that verifies accurate estimation of sensor position and orientation on the flexible tactile skin of the HRP-4C humanoid robot, and feed the calibration result into an admittance control loop[66]. This work shows that calibration is not a post-processing step of integration but a key precondition for sensing signals to enter the control loop effectively. All the mounting and interconnection schemes above assume that sensors can withstand deformation caused by the robot's own motion; when robot joints, soft structures, or skins undergo large deformation, strain coordination between sensor and body becomes the central issue determining integration success (Section 4.2).

4.2 Conformal and Stretchable Integration

Large bending, stretching, and torsion require sensors to maintain mechanical and electrical integrity while following body deformation. Conformal design involves at least three interrelated ideas: strain isolation to decouple sensing elements from bulk stretching, neutral-plane design to reduce bending strain in metal layers, and modulus gradients or soft-hard transition layers to reduce interfacial shear between flexible materials and rigid components. The first two have structural interconnect evidence; modulus gradients are still largely an unverified design direction in the current collection. None of the three, however, can replace the joint tuning of robot cycling, encapsulation, and readout.

Stretchable interconnects connect sensing elements to acquisition circuits and are among the most common paths for strain concentration and fatigue failure. Jiao et al. place a metal layer near the neutral plane of the interconnect using a Parylene-C/metal/Parylene-C sandwich, achieving mechanical integrity under 350% stretching in a curved-electronics demonstration and reporting a resistance change below 2% at 300% strain; an 8 × 8 LED array survives 100 cycles under 100% expansion[67]. These results support the design value of neutral-plane and serpentine geometry, but the validated object is LED curved electronics rather than a complete robot perception loop, and cycle count and conditions cannot be extrapolated to long-term service life. Ham et al. combine multiple flexible sensors and wire bundles on a stretchable kirigami network wrapped around a soft robotic hand[68]; this case shows that integrated fabrication of interconnects and sensors is transferable, but interface and encapsulation failure still need validation under real robot loads.

Wireless communication can reduce long leads but does not automatically remove interconnect, power, or encapsulation constraints. Liu et al. present an architectural reference for an all-flexible electronic skin with bidirectional communication via Bluetooth and Wi-Fi[69]; the result comes from a wearable scenario, and connection reliability, radio-frequency performance, and power consumption under cyclic robot deformation still require separate evaluation. Pang et al. note, from the perspectives of continuous whole-body coverage, dense interconnection, long-term durability, and environmental benignity, that uneven coverage density and cable bandwidth remain major engineering obstacles preventing large-area robot skin from moving from components to system deployment[70]. Acceptance of conformal and stretchable integration should therefore cover short-term function retention, long-term damage accumulation, wireless links, and maintenance accessibility, and connect to the energy budget of the next section.

4.3 Self-Healing and Self-Powered Integration

Flexible sensors endure cyclic loading during long-term robot operation, and material fatigue and interfacial degradation inevitably degrade sensing performance. The goal of self-healing integration is to restore mechanical integrity, conductive pathways, and sensing function together after mechanical damage; only when all three recover together does it count as repair in the sense of robot deployment. Bond recovery at the material level alone is insufficient for a system-level capability.

Dai et al. build a fully intrinsic self-healing multimodal sensor on a dynamic-bond crosslinked network (insulating polymer plus conductive hydrogel) that restores three sensing modes without external healing agents: piezoresistive strain, thermal-resistance temperature, and triboelectric self-powered sensing, and achieve conformal integration with a soft robot[60]. It is one of the few self-healing multimodal sensor systems validated in a robotic scenario. At the material and device level, Vo et al. construct a fully functional-layer autonomous self-healing transistor circuit on a unified supramolecular self-healing polymer matrix and demonstrate NAND and NOR gates[71]; Zhang et al. and Wang et al. demonstrate combinations of room-temperature self-healing with high stretchability in strain sensors and ionic conductive elastomers, respectively[72,73]. These works extend the functional boundary of self-healing at the circuit and material levels, but evaluation of sensing-function recovery under robot cyclic loading and encapsulation constraints is not yet complete. From the existing evidence, material-level progress in self-healing far exceeds system-level progress: cooperative recovery of mechanical, electrical, and sensing functions under robot cyclic conditions has only just begun in a few works.

Self-powered integration should not be judged by whether a sensor can output voltage or current, but by whether the whole system budget of energy harvesting, storage, readout, and wireless nodes can close. Triboelectric and piezoelectric devices can reduce external bias requirements at the transduction stage, but sampling, signal conditioning, computation, wireless transmission, and standby losses still need matching energy sources and timing. Evidence in the current index is mainly single-device, single-node, or material-layer demonstrations; system-level validation of multi-node energy management, distributed power supply, and long-term task operation is lacking. This section therefore assigns no unified level to output power and does not describe self-powered as energy autonomy. Before entering the closed-loop control of Chapter 5, sustained signal quality under energy-constrained conditions must be further verified.

5 Intelligent Perception and Closed-Loop Control

Chapter 4 established the mounting, interconnection, encapsulation, and calibration conditions for flexible sensors to enter a robot body. On this basis, this chapter discusses how raw resistance, capacitance, voltage, light-intensity, or wavelength sequences become state estimates and control inputs. The processing chain comprises signal correction and representation, high-level tactile recognition, multimodal fusion, and feedback control. Tactile sensing is the object with the most concentrated evidence; body deformation, proximity, and environmental physical quantities are used to test whether the same processing principles hold across information sources. Only methods that take flexible sensing data as direct input and provide robot-direct task-level evidence are included; general machine-learning or control algorithms are not treated separately.

5.1 Tactile Signal Processing and Feature Extraction

Once flexible sensors leave the calibration bench, raw outputs carry drift, crosstalk, and mounting deviations. Unless these non-idealities are corrected first, subsequent classifiers learn device defects rather than contact information. This section compares, not the names of feature algorithms, but three common preconditions: whether array readout errors are corrected before representation learning, whether hysteresis and baseline drift are modeled explicitly, and whether time-frequency and spatial representations retain an interpretable correspondence with operating conditions. Across systems, readout correction and baseline compensation are common preconditions of almost all array routes, but the compensation cost is tied to specific devices and operating conditions.

Representative evidence for readout and baseline correction comes from device-level systems (L0). Yao Li et al. combine correlated double sampling with a zero-potential method and compensate element differences with a column-parallel current DAC, achieving readout errors below 0.3 per mille for a 10 × 10 flexible resistive array, with a 180 nm CMOS chip area of 4.8 mm² and power of 285 μW[74]. Abdul-Hussain et al. train a backpropagation network on current and historical resistance to reduce the maximum hysteresis error of conductive-fiber tactile elements from 24.2% to 13.5% of full-scale output[75]; the residual error shows that data-driven compensation does not eliminate device memory effects. Time-frequency and spatial representation evidence rises to robot integration (L1). The robot skin of Sheng Li et al. scans periodic textures under about 1 N normal force and verifies texture encoding through the relation between FFT feature frequency, scanning velocity, and texture period, where 485 Hz is a feature frequency rather than end-to-end processing latency[76]. Hongyu Li et al. use graph neural networks and contrastive learning to obtain taxel representations containing geometric information, mapping low-resolution signals to high-resolution contact surfaces[77].

The highest evidence level in this section is L1, all open-loop demonstrations. Reference[74] gives no scanning bandwidth, end-to-end closed-loop latency, or long-term cyclic results for a large-area robot skin. The model of[75] depends on specific layer counts, loading sequences, and calibration data. The feature frequency of [76] cannot be interpreted apart from contact force and scanning velocity. The super-resolution metric of [77] depends

on a synthetic database, with the real robot completing only limited YCB surface classification and no closed-loop manipulation gain, inference latency, or cross-layout calibration cost reported. Studies of tactile-data super-resolution[78] and array calibration[79] further indicate that early processing constrains what later models can use; unified representations of proximity, environmental temperature and humidity, and cross-layout body signals still lack robot-task-level comparison.

5.2 Learning-Based Tactile Perception

Handcrafted features are adequate when objects are fixed and conditions are uniform, but robots facing unknown objects and dynamic environments need to discover discriminative representations from data automatically. The key comparison is not model complexity but three sets of matches: input representation (regular pressure maps, sparse taxels, multichannel time series) with network architecture, task output (regression, classification, structured prediction) with supervision target, and data-generation conditions (calibration samples, object sets, deployment conditions) with reporting style. Model performance must be reported together with data conditions; different networks cannot be compared apart from data-generation conditions.

Four pieces of evidence cover levels from bench to pre-closed-loop. Gao et al. feed the 16-channel readout of a meshless flexible planar sensor into a deep neural network; two-point pressure and position prediction errors stay within 4%, and 16-class shape recognition reaches 97.7%, but the results come from bench and manual touch-pressure data without robot-body integration (L0)[80]. Kong et al. first optimize sparse taxel topology and then use a self-attention super-resolution model to generate 2700 virtual taxels from 23 physical taxels, achieving a localization root-mean-square error of 0.73 mm and 98.35% accuracy for large-scale contact-shape classification, with inference of about 1 ms per sample. The sensor is integrated on a robot hand, but no manipulation gain such as grasp success rate is reported (L1)[81]. Zhou et al. use an LSTM on a three-finger soft gripper for object recognition, with accuracies of 98.64% for ten classes at 25 degrees Celsius, 99.0% for five classes at -20 degrees Celsius, and 90.58% for four classes under four orientations; this section uses only their recognition evidence (recognition is an L1-level demonstration; the force-control closed loop appears in Section 5.4)[59]. Lu et al. move learning into the device-design stage, screening triboelectric tactile parameters by task separability, and the optimized six-class dynamic touches reach about 99.58% accuracy with a linear SVM; after disassembly and reassembly of the same sensor, the pretrained classifier drops from 96% to 87.5% (L1)[82].

These four pieces of evidence mainly support supervised learning under specific layouts, objects, and acquisition procedures: calibration costs after changing devices, layouts, reinstallation, or environment are not systematically verified, and generalization to open object sets has no task-level evidence. The 1 ms of [81] belongs only to the shape classifier, not to the complete acquisition-reconstruction-decision chain. The three result sets of [59] differ in object counts, temperature, and posture conditions and cannot be merged into general performance. Learning-based perception as a whole remains at the level of recognition under specific conditions, and no evidence shows that it directly improves downstream manipulation.

5.3 Multimodal Fusion

Tactile sensing alone can answer what was contacted, but not where the object is or what configuration the robot is in; vision and body-state sensing also have their own blind spots. The cross-cutting comparison dimension of fusion is the information gap in the task: vision provides pre-contact location and appearance, proximity supplements near-field warning, flexible tactile sensing provides post-contact pressure, thermal properties, texture, and slip, and body state constrains pose and action history. Evaluation must report single-modality baselines, temporal alignment, spatial correspondence, and task-level results together, rather than comparing by input-channel count or fusion-model name.

By processing level and evidence grade, four systems validate fusion gains at the decision, feature, model, and policy layers. Mao et al. use binocular vision for localization and flexible tactile sensing for temperature, thermal conductivity, pressure, texture, and slip on a household robot; on a closed set of ten daily objects, tactile-vision recognition accuracy reaches 96.5%, higher than 59% for vision-only and 92% for tactile-only, and slip feedback enters grasping control (L2) [7]. Ding et al. use adaptive dropout to weight tactile-vision fusion by sample quality, reaching 99.3% category accuracy and 97.8% material-attribute accuracy on 27-class grasping data with stronger robustness under visual occlusion, but without a closed-loop task (L1) [83]. The SPOTS system of Mandil et al. keeps separate visual and tactile prediction pipelines, with the largest joint-prediction gain on objects that look identical but differ in physical properties, and tactile predictions flatten after visual occlusion (L1)[84]. Li et al. feed wrist vision, tactile images, marker deviations, and body state into a diffusion policy, reaching 85.5% average success across five real tasks, higher than 66.3% for tactile-only and 55.4% for vision-only; the policy actually runs at 30 FPS and cannot be represented by the sensor nominal rate of 120 Hz (L3)[85].

The fusion gain depends on whether the task contains physical ambiguity that a single modality cannot remove: when object dynamics can be inferred from vision[84], the gain is limited;[83] does not show handling of dynamic slip, unknown objects, or failed grasps; [7] mixes the contributions of sensing, cascaded recognition,

and task rules and does not validate open objects or cross-household operation. Existing datasets are mostly task-specific and depend on specific sensors; unified benchmarks and standardized protocols remain insufficient[86]. Task-level evidence for pre-contact/post-contact synergy between proximity and tactile sensing, and for environmental physical quantities entering fusion, is even scarcer.

5.4 Closed-Loop Control Enabled by Flexible Sensing

The preceding three sections address how signals are read, recognized, and fused; what the robot ultimately needs is a change in action. Once flexible sensing enters a closed loop, the key comparison is no longer whether contact can be distinguished, but how the sensed quantity defines the controlled state, when the controller updates, and how the actuator changes contact. Evaluation must separate device response time, signal-processing latency, control period, and task completion time, and report calibration, saturation, failure modes, and safe fallback. A single grasping demonstration or classification accuracy cannot replace closed-loop tracking error.

Four control structures cover continuous regulation, event triggering, and pose search. Zhou et al. drive a PID controller with the error of fingertip capacitive tactile output on a three-finger soft gripper, regulating air pressure through proportional valves; after tuning on a 450 g Ecoflex bottle, the rise time is 11.6 s and the steady-state error 3.44%, with the loop actually controlling capacitance rather than force directly (L2) [59]. Sekine et al. detect slip with a flexible ferroelectric shear sensor and command an electromagnetic valve to add 30 kPa for regrasping by a pneumatic soft gripper when the threshold is exceeded; both sensor response times are below 50 ms, but the full-loop latency also includes PC, converter, valve, air path, and gripper dynamics (L2) [87]. Low et al. compute grasp-instability from the covariance and variance of three-finger force signals and close the loop by exploring three candidate postures in sequence, selecting the most stable one; they report 100% grasp success in 10 trials each for tomato, potato, and broccoli, with force signals sampled at 50 Hz but each candidate posture held for 5 s (L3) [88]. Min et al. fuse pneumatic skin with motor-current proprioception to estimate contact force, use a temporal convolutional network (TCN) to compensate static friction and stick-slip transitions, reduce the dead zone by 53.86% relative to the uncompensated baseline, and achieve compliant interaction and kinesthetic teaching through admittance control (L2)[89].

Closed-loop task evidence concentrates on centralized supervisory loops. The parameters of Zhou [59] depend on the sensor, contact area, and air path. The threshold of Sekine [87] is not calibration-free across objects. Low [88] demonstrates task-level grasp-posture search rather than high-frequency contact-force tracking and cannot be extrapolated to unknown or contaminated objects. Min [89] shows degraded estimation reliability when transitioning from dynamic motion to rest, reporting only the about 400 Hz motor communication frequency without a complete perception-estimation-control period. Cross-system comparison should track nine conditions along the same chain (Table 3 summarizes cross-layer evidence from new observable to evidence level by application direction): new observable, transduction and sensing topology, mechanical and electrical interfaces, calibration and drift, sampling and full-chain latency, energy and maintenance, task gain, failure fallback, and evidence maturity. Most existing cases aggregate signals to a supervisory controller, and distributed local sensing-actuation loops have not been validated, so their bandwidth, fault tolerance, and wiring benefits cannot be compared. Chapter 6 uses this condition set to evaluate specific robot tasks.

6 Applications: Capabilities Enabled by Flexible Sensing

Chapters 3 to 5 explain how flexible sensing signals are generated, how they enter the robot body, and how they become estimates and control inputs. This chapter uses robot tasks as the evaluation unit (Fig. 4 shows representative real-robot systems for the three task domains) and tracks whether the three types of information, contact interface, body configuration, and near-field environment, produce verifiable gains. Device performance constitutes evidence of application value only when it can explain the added observable, the processing and control approach, the real-robot result, and the failure boundary.

6.1 Contact-Force Sensing and Dexterous Manipulation

The increment that flexible sensing brings to dexterous manipulation should be judged by whether it prevents crushing or dropping, identifies contact states, and completes the task, not by device sensitivity alone. Systems to be compared must state, in sequence, the task bottleneck, the new observable added by the sensor, the feedback action, the real-robot result, and the failure boundary: local normal force is used to limit gripping load, tangential force and friction changes identify slip, and distributed contact or tactile images supplement shape and load location.

For fragile or slippery objects, the key increment is separating normal load bearing from tangential instability. Liu et al. decouple normal pressure from shear force with centrosymmetric and axisymmetric microstructures (Fig. 4a); during orange grasping, a drop in the sensing response triggers an increase in grip force, achieving damage-free grasping (L2) [6]. The soft triaxial optical force sensor of Mo et al. detects slip of a plastic

Table 3 Cross-layer evidence matrix from observables to evidence levels

New observable	Body integration	Calibration & drift	Sampling/end-to-end latency	Control use	Task-level result	Failure boundary	Evidence level	Reference
Normal/shear decoupling (centro-/axisymmetric struct.)	Robotic hand tip	Calib. n.r.	Not reported	Grip-force increase on signal drop	Damage-free orange grasp	Single orange case, no repeats	L2	[6]
Triaxial force (2.88 V/N) + tangential slip	Dexterous hand, LED-PD soft optical unit	Calib. n.r.	22 ms (sensor); end-to-end n.r.	GRU slip detection → increase bending angle	Stable grasp after slip	Plastic container only; no success rate/loop latency	L2	[50]
Pressure/thermal/texture/slip (limit 0.05 mm/s) + binocular vision	Household robot, hierarchical sensing-decision	Calib. n.r.	4 ms (sensor), not task cycle	Slip-feedback grasp + cascade	Recognition 96.5% vs 59%/92%	Closed 10-class set; no open objects/cross-household	L2	[7]
Ionic-hydrogel strain + tactile (capacitive readout)	Three-finger gripper + arm + LCR readout	PID tuned per contact/pneumatics	11.6 s (PID rise time)	PID force control + slip compensation	Recognition 98.64/99.0/90.58%, force err 3.44%	Fingertip-only contact loses slip signal; regrasp after drop	L2	[59]
PAM length (spring-inductor)	PAM + tendon-driven flexible arm	Sensing error 1.16 ± 0.75 mm	Not reported	Length-feedback closed loop	Steady-state error 5 → 2 mm (open→ closed loop)	Single sensor cannot separate bending from elongation	L2	[90]
Cable-error compensation + segment tracking (encoders + onboard vision)	Multi-segment continuum robot	Calib. n.r.	3 Hz (visual feedback)	Two-level closed-loop shape control	Distal mean error 6.50 → 1.72 mm	Vision 3 Hz; occlusion and high-speed motion limited	L2	[53]
FBG 3-D configuration (online model)	Soft manipulator (embedded FBG)	Calib. n.r.	Not reported	Online model → shape servoing	Errors re-converge under collision/loads	Variable arc length not estimated; no repeats	L2	[91]
SAW touch localization (96.4% <2 cm) + pressure estimation	Jaco arm + piezo transducer pair	New surface → OSPA recalibration + retraining	Not reported	Open-loop demo, no control driving	No task closed loop (localization/force estimation only)	Motion vibration raises error (pressure RMSE 1.86 vs 0.59 N)	L1	[92]
Distributed contact (11 AIRSKIN pads)	UR10e + 11 AIRSKIN pads	Pad sensitivity varies; effective mass from dynamics model	25 Hz (threshold update)	Adaptive threshold → STOP/AVOID	Task time 9.96 → 7.28 s, 9.98 → 5.97 s	3 real collisions/condition; in-situ measurements needed	L2	[93]
Multi-axis contact force (skin cues + motor current)	4-DoF platform + pneumatic skin + motor-current proprioception	Calib. n.r.	≈400 Hz (motor comm.); full cycle n.r.	Admittance control + TCN compensation	Static-friction dead zone reduced 53.86% (vs baseline)	Reliability drops at motion-to-rest; platform-specific	L2	[89]
Slip shear signal (flexible ferroelectric)	Pneumatic soft gripper (D/A → valve → air path)	Threshold calibrated per object/friction/grip state	<50 ms (sensor); loop latency n.r.	Slip threshold → +30 kPa → regrasp	Automatic regrasp after slip (multiple objects)	Threshold not calibration-free across objects	L2	[87]
Whole-body tactile + proximity (GenTact-Prox)	Franka arm + modular 3D-printed whole-body units	Calib. n.r.	Not reported	Proximity → deceleration obstacle avoidance	Deceleration after detecting human-hand trajectory	Single robot/skin configuration only	L2	[62]

Note: Latency: Mo 22 ms, Mao 4 ms, Sekine <50 ms (sensor); Fang 3 Hz; Rustler 25 Hz; Zhou 11.6 s; Min ≈400 Hz; full cycle n.r. Task-level results are task metrics only; sensing/reconstruction accuracy is under "New observable" or "Calibration & drift". Per Table 1: L1 = open-loop demonstration on a robot; L2 = closed-loop task. Fang 2023 is the L1 baseline; others L2. PID = proportional-integral-derivative; LCR = inductance-capacitance-resistance; OSPA = optimal sub-pattern assignment; LED-PD = light-emitting diode-photodiode pair; n.r. = not reported; other abbreviations as defined in the text; STOP/AVOID = collision-reaction tasks in [93]; AIRSKIN = sensitive-skin system in [93].

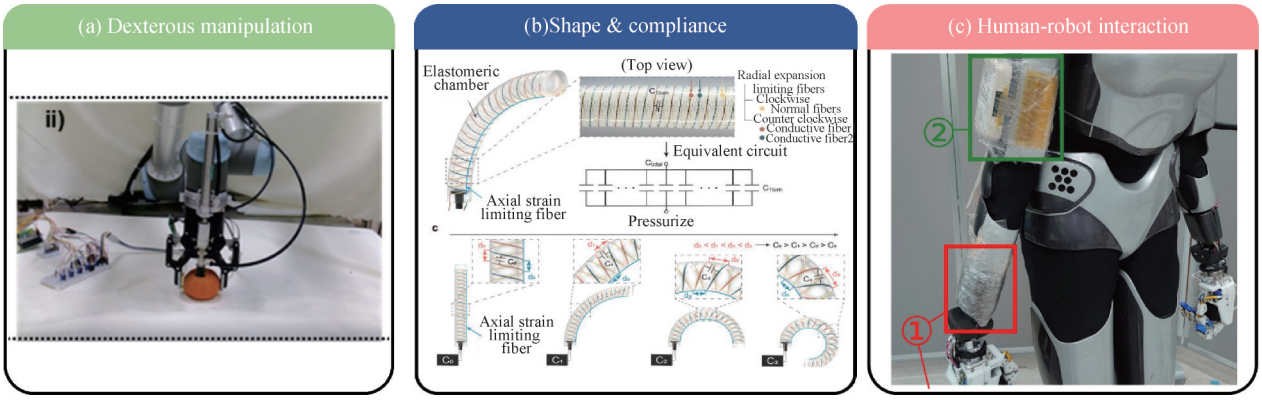


Fig.4 Three representative robot systems enabled by flexible sensing. (a) Dexterous manipulation: a flexible tactile sensor with centro-/axisymmetric microstructures decoupling normal pressure and shear force is mounted at a robotic hand tip, where slip recognition during orange grasping triggers a grip-force increase for damage-free grasping[6]. (b) Shape and compliance sensing: a soft actuator with radial-expansion-limiting fibers reconstructs axial strain and bending configuration from microfiber capacitance changes[15]. (c) Human-robot interaction: a flexible tactile skin on the wrist of the HRP-4C humanoid robot enters an admittance control loop after spatial calibration[66]. (a) Adapted from[6], (b) from[15], and (c) from[66], all under CC BY 4.0.

container through tangential-force feedback, and the dexterous hand restores a stable grasp after increasing the bending angle twice (L2)[50]. The two works jointly verify the real-robot chain of slip, force increase, and stabilization, but the objects are limited to an orange and a plastic container, respectively, and neither reports task success rates or complete closed-loop latency. End-to-end systems also need to connect post-contact information with pre-contact localization. Mao et al. use vision to determine object position and pose, with flexible tactile sensing providing pressure, thermal properties, texture, and slip. Their slip-detection lower limit is 0.05 mm/s with a 4 ms sensing response; tactile-vision recognition accuracy for ten daily objects is 96.5%, and autonomous tabletop classification and cleaning are completed (L2) [7]. The 4 ms, however, is a sensor response, not a complete task cycle. The three-finger soft gripper combining hydrogel tactile sensing with force control is a representative real-robot system of this chain, and its closed-loop control is discussed in Section 5.4[59].

High-dimensional contact estimation has not yet translated into task gains. The 9DTact system of Lin et al. is trained on 100,417 image-force pairs and, under object-held-out validation, achieves mean absolute errors of 0.370 N for force and 0.0077 N-m for torque in six-dimensional force estimation. Generalization, however, covers only unseen objects on the same sensor. No downstream manipulation task demonstrates that the error improvement improves grasping or assembly, and the evidence level remains L0, outside the task loop[94]. Existing cases also do not quantify force distribution among fingers or contact redirection, and the cleaning demonstration lacks repeated success rates, open objects, and cross-household operation evidence.

6.2 Deformation Sensing and Compliant Control

Soft and continuum robots lack the well-defined configuration that rigid joints provide, and actuation inputs are also affected by material hysteresis, cable elongation, inter-segment coupling, and external contact. The task increment of deformation sensing is not to provide local strain values but to reconstruct length, curvature, or three-dimensional shape that can be used for control, and to convert state errors into actuation corrections within the feedback bandwidth; evaluation must distinguish shape-measurement error, control error, and task outcome. The microfiber capacitive strain sensor conformally attached to a soft body (Fig. 4b) is a representative device route carrying the mapping from local strain to global shape[15].

Low-dimensional sensing suits a single deformation closed loop, while multi-source systems handle coupled states. Sahu et al. use a spring-inductor sensor to feed back the length of a pneumatic artificial muscle, with a measurement error of 1.16 ± 0.75 mm; on a tendon-driven flexible arm, the closed loop reduces the mean steady-state error from 5 mm (open loop) to 2 mm (L2) [90]. Fang et al. compensate cable error with rotary/linear encoders and track each segment of a multi-segment continuum robot with onboard vision, reducing the mean distal error from 6.50 mm to 1.72 mm (L2)[53], although the visual feedback runs at only 3 Hz and occlusion and high-speed motion remain limited. High-density FBG reconstructs global shape from local wavelength shifts and closes the servo loop: Lu et al. drive shape servoing with FBG three-dimensional configuration feedback and online model learning, re-converging errors under collisions, unknown loads, and colonoscope and oropharyngeal-swab phantoms (L2) [91]. A model-free fuzzy logic controller closes the loop on a three-section, six-degree-of-freedom continuum robot with only end-position and orientation feedback, achieving trajectory-tracking root mean square errors of 0.31-1.00 mm (0.19% -0.60% of robot length) [95]. A unified neural network further corrects FBG-based distal positions across two continuum robots and multiple fiber configurations from

camera-tracked ground truth, implicitly compensating twist and placement errors and reducing worst-case errors by up to an order of magnitude at >100 Hz[96], but shape sensing still does not estimate variable arc length.

Sensing and servoing must be separated: the learned shape reconstruction of Ha et al. has errors of 0.24 mm and 0.49 mm in free and constrained space, respectively, and runs at 200 Hz, but the experiments use open-loop actuation and do not form a task loop; the training ground truth relies on a constant-curvature assumption and does not cover S-shaped bending (L1) [49]. Ferguson et al. jointly estimate shape and external load, with mean errors of 0.07 N and 7.5 mm for point-load magnitude and position and a 4.1 mm RMS position error for the tendon-driven prototype shape, but the MATLAB prototype takes 4.01 s on average and cannot yet be used for real-time closed loop (L1)[97]. Deformation-feedback routes should be selected by observable state, spatial coverage, ground truth and model assumptions, bandwidth, and closed-loop benefit, not ranked by sensor accuracy alone.

6.3 Human-Robot Interaction Safety and Intent Understanding

In shared human-robot spaces, flexible sensing serves pre-contact safety, post-contact safety, and active interaction: proximity provides near-field warning before collision, large-area tactile sensing detects contact location and local action intensity, and body state distinguishes external forces from the robot's own motion. Current real-robot evidence concentrates on post-contact tactile localization, collision response, and physical guidance; closed-loop task evidence for pre-contact proximity and environmental physical quantities is markedly scarcer. Evaluation should separate localization and force estimation, collision response, and interaction task outcomes, and single-sensor accuracy cannot replace safety or intent-understanding capability. The whole-body robot skin built from distributed modules and multilayer fabrics provides a system basis for large-area contact coverage[63], and spatial calibration of a flexible tactile skin after mounting on complex curved surfaces (Fig. 4c) is a precondition for contact localization to enter the control loop[66].

Three levels of evidence represent perception demonstrations, response-threshold regulation, and compliant control, respectively. Fan et al. mount only a pair of piezoelectric transducers on a Jaco arm and use surface acoustic waves propagating in the body to localize touches and estimate pressure. During arm motion, 96.4% of touch-localization errors remain below 2 cm; pressure-estimation RMSE is 0.59 N at rest and 1.86 N in motion (L1; localization and force estimation are perception demonstrations) [92]. Rustler et al. update the threshold of each skin pad at 25 Hz on a UR10e covered by 11 AIRSKIN pads according to link velocity and effective mass; in real pick-and-place, the effective-mass strategy reduces STOP from 9.96 s to 7.28 s and AVOID from 9.98 s to 5.97 s (L2)[93]. Min et al. apply the admittance-control loop analyzed in Section 5.4 to grasp guidance and non-grasp kinesthetic teaching (L2)[89].

Existing evidence supports collision detection, touch localization, and physical guidance, but is insufficient for general social-tactile category recognition or bidirectional tactile communication. Reference[92] depends on specific surface propagation properties; changing materials requires a fresh single-shot calibration, online feature update, and classifier retraining, and errors grow during motion. In[93], each condition has only three real collisions and pad sensitivities are inconsistent; adaptive thresholds improve continuous operation but cannot replace safety certification and real-robot mechanical verification. Reference[89] shows degraded estimation reliability when transitioning from dynamic motion to rest and does not report a complete perception-estimation-control period.

Across the three application domains, contact detection, slip feedback, and grasp regulation under limited objects already form a fairly complete real-robot chain; shape reconstruction and compliant control are advancing from state estimation toward closed-loop validation; and proximity, ambient temperature and humidity, and cross-platform whole-body sensing still lack unified task and long-term deployment evidence. The maturity differences among the three routes stem mainly from whether spatial coverage, cross-surface calibration, full-chain bandwidth, energy and maintenance, and failure fallback are validated together, rather than from any single device metric.

7 Challenges and Outlook

The preceding six chapters traced the evidence chain of flexible sensing entering robot tasks along materials, integration, signal processing, and closed-loop control. Overall, contact tactile sensing has formed a relatively complete real-robot closed loop under limited objects, body-deformation sensing is advancing from state estimation to task-level validation, and environmental sensing and cross-platform whole-body deployment remain at the device-demonstration stage. Fig. 5 summarizes the main system-level challenges and future research paths; its left column of five challenges, middle column of the minimum reporting set, and right column of two future paths correspond to the elaboration in Sections 7.1-7.4.

7.1 Five Gaps Between Device Performance and System Reliability

The gap from device to system concentrates into five gaps that are coupled and amplify progressively. First, the accuracy-robustness trade-off: microstructure engineering amplifies sensitivity while worsening hysteresis and fatigue, and the more extreme the sensitivity metric, the higher the cyclic-service risk. Multilayer hemispherical

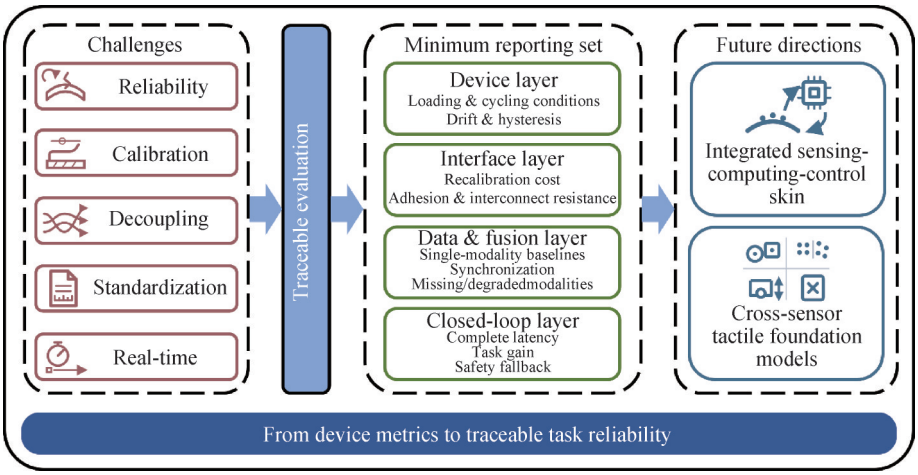


Fig.5 Convergence from device metrics to traceable task reliability. Left column: five system-level challenges—cyclic reliability, calibration, multi-physical decoupling, evaluation standardization and real-time performance. Middle column: four-layer minimum reporting set under "traceable evaluation"—device layer (loading/cyclic conditions, drift and hysteresis), interface layer (adhesion and interconnect resistance, recalibration cost), data and fusion layer (single-modality baselines, time synchronization, missing or degraded modalities), and closed-loop layer (full latency, task gains, safe fallback). Right column: two complementary future paths—sensing-computing-control integrated intelligent skin and cross-sensor, cross-task tactile perception foundation models.

microstructures report 7.66 kPa^{-1} sensitivity over 0-583 kPa, but validation is limited to wearable scenarios, the evidence level is L0, and lifetime data under robot cyclic loading remain far from sufficient[26]; joint reporting of sensitivity and lifetime is almost absent in the current literature. Second, the integration interface: modulus mismatch, interfacial delamination, and interconnect fatigue degrade device performance after integration. The whole-body skin case has completed modular integration and entered collision-avoidance control at evidence level L2, but validation covers only a single robot and a single skin configuration[62]. The rigid-island capacitive array drifts upward by 6.5% in the unloaded baseline after 3000 force cycles, and passing device-level tests does not remove drift and recalibration costs[39]. The 350% stretching and 100-cycle validation of serpentine interconnects targets LED curved electronics rather than a complete perception loop, at evidence level L0[67]. Cross-platform calibration costs have not been systematically quantified. Third, multiphysical decoupling: force-temperature-humidity coupling on a shared flexible substrate already has ideas such as frequency-domain decoupling at the device level, but that validation comes from a non-robotic scenario at L0[23], and decoupling validation under robot task conditions is lacking. Fourth, reporting standardization: different systems report performance with inconsistent force ranges, loading rates, and cyclic conditions, so cross-system comparison cannot rule out test-condition confounding; fabric-route sensitivity numbers are not comparable because physical quantities, areas, and loading conditions differ[30,32], and the lack of unified benchmarks has become a major obstacle to system comparison[86]. Fifth, closed-loop latency: full-chain latency from acquisition to actuator response is rarely reported completely. The PID force-control loop has an 11.6 s rise time and 3.44% steady-state error, loop-level metrics under single-object tuning[59]; in the slip-triggered loop, the sensor response is below 50 ms, but the link latency contributed by the PC, converter, valve, air path, and gripper dynamics is not reported[87]. Distributed local sensing-actuation loops still lack real-robot evidence.

According to the grading statistics of this review, none of the 97 papers provides peer-reviewed L4 evidence (cross-platform, long-term, or real-environment deployment). This gap is itself the conclusion: the common root of the five gaps is that validation always remains outside deployment conditions.

7.2 A Minimum Reporting Set for Flexible Sensing Research

Row-by-row checks of Tables 2 and 3 show that the not-reported items in the current literature concentrate on six types of information, each corresponding to one of the gaps in Section 7.1. The minimum reporting set needed for submission therefore covers six items. First, operating-condition range: force/pressure range and loading rate, so that sensitivity and measuring range are reproducible. Second, cycle count and lifetime: loading frequency, number of cycles, and post-cycle drift, replacing vague statements of validated durability. Third, drift and recalibration cost: baseline change, and the samples and cost of recalibration after reinstallation or environmental change. Fourth, layered end-to-end latency: sensing response, algorithm frequency, control period, and task duration reported separately, avoiding device response time masquerading as link latency. Fifth, failure fallback: safe behavior under saturation, disconnection, or calibration failure. Sixth, evidence level: validation location labeled L0-L4, so that deployed and demonstrated cannot be confused.

This set is not a new threshold but a natural

extension of the standardization tradition in instrumentation: metrological traceability and uncertainty reporting are basic norms in this field, review-level warnings about long-term performance degradation caused by environmental factors have existed for some time[4], and the absence of unified benchmarks is the main obstacle to current system comparison[86]. All the items above can be added at low cost using existing experimental conditions: the set does not require unified test equipment, only that test conditions and validation boundaries be written down so that conclusions from different works can be compared on the same coordinates. As an enforceable submission requirement for a journal, it can drive convergence of the evidence chain more effectively than any single performance metric.

7.3 Integrated Sensing-Computing-Control

Converging sensing, computation, and control onto the same physical surface is a candidate path for relieving the latency and interconnect gaps of Section 7.1, and current progress concentrates on three levels. In-memory/near-sensor computing: capacitive in-memory computing has completed noise suppression and edge detection at the sensing end, with single sensing-computing operations consuming more than 22x less power than conventional digital-analog hybrid systems[41]; this gain, however, is device evidence at the sensing-computing unit level (L0), cannot be written directly as whole-robot energy savings, and its readout bandwidth, cross-device consistency, and robot-task validation are still missing. Self-powered system budget: self-healing and self-powered integration mostly stops at the material and single-device level, with only an isolated conformal-integration demonstration[60] validated in robotic scenarios and the rest remaining at circuit or material level[71-73]; energy harvesting, storage, readout, and wireless nodes must form a closed system budget, and self-powering at the transduction stage cannot replace node-level energy autonomy. Distributed local sensing-actuation loops: the conclusion of Section 5.4 shows that most existing closed loops aggregate signals to a supervisory controller; loops in which local sensing directly drives local actuation have not been verified on real robots, and their bandwidth, fault-tolerance, and wiring benefits remain speculative.

The whole-body skin case has shown the feasibility of modular sensing with edge access[62], but there are no cross-platform data on how computation location, communication bandwidth, and energy budget scale with coverage area. It should be clear that none of these directions substitutes offline accuracy or unit-level power advantages for closed-loop and long-term deployment evidence; acceptance still rests on task gains and the system budget.

7.4 Model Transfer Across Sensors and Tasks

Learning-based tactile perception currently holds only within specific layouts, objects, and acquisition procedures, and the transfer gap is directly visible at four evidence points. First, after disassembly and reassembly of the sensor, the pretrained classifier accuracy drops from 96% to 87.5% and requires fine-tuning on a small amount of new data to recover[82], showing that the model is deeply bound to calibration samples. Second, the sparse-array super-resolution model guides new device design, but whether the same trained model transfers across devices and layouts is not verified[81]. Third, the object-held-out validation of six-dimensional force estimation covers only unseen objects on the same sensor[94]. Fourth, the object sets of temporal recognition are fixed (10/5/4 classes) [59]. The absence of unified benchmarks makes it difficult to position these gaps horizontally[86].

Transfer validation can accordingly be divided into three levels, each with explicit acceptance conditions. Same device, different tasks: report the amount of data shared between tasks and the performance retention after transfer, proving that what transfers is the representation rather than the labels. Same task, different devices: report the fine-tuning sample size after reinstallation or recalibration, the accuracy-recovery curve, and end-to-end latency. Cross-platform: repeat trials across robot bodies and sensor types in real environments, meeting L3-L4 evidence requirements. The idea of using a unified tactile representation as a candidate foundation-model path is consistent with this view, but the foundation model is currently a research hypothesis rather than a verified capability: it must first be shown that a unified representation across sensor data preserves calibration traceability, and then be validated through real-task closed loops, before it can enter the robot evidence chain.

8 Conclusions

Combining the analysis of the preceding six chapters and this chapter, the next steps of the field should converge along three main lines. First, comparable evaluation under unified conditions: compare sensitivity, drift, and lifetime with consistent force ranges, loading rates, and cyclic conditions, consistent with the evidence grading of Section 1.1 and the abstract. Second, reporting of end-to-end latency and maintenance cost: complete the not-reported items of Tables 2 and 3 according to the minimum reporting set of Section 7.2, making layered latency, recalibration cost, and failure fallback routine acceptance items. Third, perception-decision-action loops with fail-safe fallback: contact tactile sensing has formed a relatively complete real-robot closed loop under limited objects and conditions, with L3 evidence marked by repeated-trial statistics[85,88], but environmental sensing, cross-platform transfer, and long-term whole-body deployment still lack unified validation, and none of the 97 papers provides peer-reviewed L4 evidence.

These priorities translate into a time-phased

roadmap. In the short term (one to three years), the field needs benchmarking before novelty: adoption of the minimum reporting set of Section 7.2, unified test conditions for sensitivity, drift, and lifetime, and open protocols that separate device response from end-to-end task latency. In the medium term, validation must extend across platforms, sensors, and tasks, so that models and thresholds are retrained and recalibrated under documented costs rather than rebuilt from scratch. In the long term (five years and beyond), the target is deployment-grade evidence: whole-body sensing under environmental variation, maintenance-aware operation, and safety certification, which together correspond to L4 evidence rather than additional device-level metrics. Short-term benchmarking is therefore not a bureaucratic detour but the precondition for any credible long-term deployment claim.

The next priority of the field is not to continue improving individual sensitivity in isolation, but to build traceable, comparable, and maintainable system evidence for perception, judgment, and action. Only when device metrics, interface conditions, latency budgets, and failure behavior are placed in the same reporting and acceptance framework can flexible sensing move from demonstration to deployment.

Author Contributions:

Hongxi Yang: Conceptualization, Methodology, Investigation, Data curation, Visualization, Writing - original draft, and Writing - review & editing. Shuai Xian: Formal analysis, Validation, and Visualization. Xin Dong: Supervision and Writing - review & editing. Chengcai Wang: Supervision and Writing - review & editing. Yong Zhong: Supervision, Project administration, Funding acquisition, and Writing - review & editing. All authors have read and agreed to the published version of the manuscript.

Acknowledgments:

The authors have no acknowledgments to declare.

Funding Information:

This work was supported in part by the National Natural Science Foundation of China under Grant 62473161, 52539005; in part by the GJYC program of Guangzhou under Grant 2024D03J0005, and in part by Major Science and Technology Project of the Ministry of Water Resources (SKS-2025049), and in part by the Technology Innovation Center for Basin-wide Perception and Intelligent Regulation of Water Network in the Guangdong-Hong Kong-Macao Greater Bay Area, Ministry of Water Resources.

Data Availability:

The authors declare that the main data supporting the findings of this study are available within the paper and its Supplementary Information files.

Conflicts of Interest:

The authors declare no competing interests.

Ethics Statement:

Not applicable.

Use of Generative AI and AI-Assisted Technologies:

The authors declare that generative AI and AI-assisted technologies were used only for literature investigation and language polishing during the preparation of this manuscript. The authors have reviewed and edited the output and take full responsibility for the content of the published article.

References

[1] Hegde C., Su J., Tan J. M. R., *He K.,* Chen X., & Magdassi S. (**2023**). Sensing in Soft Robotics. ACS Nano, 17(16), 15277-15307. doi:10.1021/acsnano.3c04089.

[2] Niu H., Yin F., Kim E.-S., Wang W., Yoon D.-*Y.,* Wang C., Liang J., Li Y., & Kim N.-Y. (**2023**). Advances in flexible sensors for intelligent perception system enhanced by artificial intelligence. InfoMat, 5(5), e12412. doi: 10.1002/inf2.12412.

[3] Nong H., Jin M., Pan C., Zhou H., Zhang C., Pan X., Chen Y., Wei X., Lu Y., Zhao K., Huang M., Li X., Yu Y., & Zhang Z. (**2024**). Intelligent Sensing Technologies Based on Flexible Wearable Sensors: A Review. *IEEE Sensors Journal,* 24(14), 22197-22217. doi:10.1109/JSEN.2024.3405173.

[4] Pyo S., Lee J., Bae K., Sim S., & Kim J. (**2021**). Recent Progress in Flexible Tactile Sensors for Human - Interactive Systems: From Sensors to Advanced Applications. *Advanced Materials,* 33(47), 2005902. doi:10.1002/adma.202005902.

[5] Ren M., Wu Q., & Huang X. (**2025**). Flexible tactile sensors inspired by bio-mechanoreceptors. *Biosensors and Bioelectronics,* 267, 116828. doi:10.1016/j.bios.2024.116828.

[6] Liu Y., Cui S., Wei J., Li H., Hu J., Chen S., Chen Y., Ma Y., Wang S., & Feng X. (**2022**). Centrosymmetric - and Axisymmetric-Patterned Flexible Tactile Sensor for Roughness and Slip Intelligent Recognition. *Advanced Intelligent Systems,* 4(1), 2100072. doi: 10.1002/aisy.202100072.

[7] Mao Q., Liao Z., Yuan J., & Zhu R. (**2024**). Multimodal tactile sensing fused with vision for dexterous robotic housekeeping. *Nature Communications,* 15(1), 6871. doi: 10.1038/s41467-024-51261-5.

[8] Massari L., Fransvea G., D'Abbraccio J., Filosa M., Terruso G., Aliperta A., D'Alesio G., Zaltieri M., Schena E., Palermo E., Sinibaldi E., & Oddo C. M. (**2022**). Functional mimicry of Ruffini receptors with fibre Bragg gratings and deep neural networks enables a bio-inspired large-area tactile-sensitive skin. *Nature Machine Intelligence,* 4(5), 425-435. doi: 10.1038/s42256-022-00487-3.

[9] Meng X., Cheng L., & Li Z. (**2025**). A Tactile-Proximity Dual-

Mode Photoelectric Sensor: Implementation and Applications. *IEEE Transactions on Robotics,* 41, 6607-6624. doi:10.1109/TRO.2025.3629784.

[10] Lo Preti M., Bernabei F., Nardin A. B., & Beccai L. (**2024**). Triaxial 3-D-Channeled Soft Optical Sensor for Tactile Robots. *IEEE Sensors Journal,* 24(17), 27956-27965. doi: 10.1109/JSEN.2024.3425835.

[11] Mascia A., Spanu A., Bonfiglio A., & Cosseddu P. (**2023**). Multimodal force and temperature tactile sensor based on a short-channel organic transistor with high sensitivity. *Scientific Reports,* 13(1), 16232. doi: 10.1038/s41598-023-43360-y.

[12] Kohlbrenner C., Murray M., Zhang Y., Escobedo C., Dunnington T., Stevenson N., Correll N., & Roncone A. (**2024**). A Machine Learning Approach to Contact Localization in Variable Density Three-Dimensional Tactile Artificial Skin. arXiv preprint arXiv: 2412.*00689* . doi: 10.48550/arXiv.2412.00689.

[13] Wang Y., Wu H., Xu L., Zhang H., Yang Y., & Wang Z. L. (**2020**). Hierarchically patterned self-powered sensors for multifunctional tactile sensing. *Science Advances,* 6(34), eabb9083. doi:10.1126/sciadv.abb9083.

[14] Karipoth P., Christou A., Pullanchiyodan A., & Dahiya R. (**2022**). Bioinspired Inchworm- and Earthworm - like Soft Robots with Intrinsic Strain Sensing. *Advanced Intelligent Systems,* 4(2), 2100092. doi:10.1002/aisy.202100092.

[15] Kim H., Na H., Noh S., Chang S., Kim J., Kong T., Shin G., Lee C., Lee S., Park Y.-L., Oh S., & Lee J. (**2024**). Inherently integrated microfiber-based flexible proprioceptive sensor for feedback-controlled soft actuators. *npj Flexible Electronics,* 8 (1), 15. doi:10.1038/s41528-024-00302-6.

[16] Naik V., Fairchild P., & Tan X. (**2025**). Nonlinear compensation of stretchable strain sensors with application to proprioceptive sensing of soft robotic arm. *Smart Materials and Structures,* 34(3), 035018. doi: 10.1088/1361-665X/adb2c7.

[17] Wang P., Xie Z., Xin W., Tang Z., Yang X., Mohanakrishnan M., Guo S., & Laschi C. (**2024**). Sensing expectation enables simultaneous proprioception and contact detection in an intelligent soft continuum robot. *Nature Communications,* 15 (1), 9978. doi:10.1038/s41467-024-54327-6.

[18] Zou S., Picella S., de Vries J., Kortman V. G., Sakes A., & Overvelde J. T. B. (**2024**). A retrofit sensing strategy for soft fluidic robots. *Nature Communications,* 15(1), 539. doi: 10.1038/s41467-023-44517-z.

[19] Zhou Z., Zhang Y., Bai J., Zhang W., Wang H., & Pu W. (**2024**). Bioinspired Flexible Capacitive Sensor for Robot Positioning in Unstructured Environments. *ACS Applied Materials & Interfaces,* 16(13), 16589-16600. doi: 10.1021/acsami.4c00699.

[20] Liu Z., Chen D., Ma J., Wang T., Jia D., & Liu Y. (**2024**). Multimodal capacitive proximity sensing array with programmable spatial resolution and dynamic detection range. *Sensors and Actuators A: Physical,* 370, 115279. doi: 10.1016/j.sna.2024.115279.

[21] Alshawabkeh M., Alagi H., Navarro S. E., Duriez C., Hein B., Zangl H., & Faller L. -M. (**2023**). Highly Stretchable Additively Manufactured Capacitive Proximity and Tactile Sensors for Soft Robotic Systems. *IEEE Transactions on Instrumentation and Measurement,* 72, 1-10. doi: 10.1109/TIM.2023.3250232.

[22] Liu W., Duo Y., Liu J., Yuan F., Li L., Li L., Wang G., Chen B., Wang S., Yang H., Liu Y., Mo Y., Wang Y., Fang B., Sun F., Ding X., Zhang C., & Wen L. (**2022**). Touchless interactive teaching of soft robots through flexible bimodal sensory interfaces. *Nature Communications,* 13(1), 5030. doi: 10.1038/s41467-022-32702-5.

[23] Ma Z., Zhang J., Li J., Shi Y., & Pan L. (**2020**). Frequency-Enabled Decouplable Dual-Modal Flexible Pressure and Temperature Sensor. *IEEE Electron Device Letters,* 41(10), 1568-1571. doi:10.1109/LED.2020.3020937.

[24] Zhang C., Lang S., Tao M., Li P., Liang T., Zhao X., Gou X., Zhao X., Xiong S., Zheng L., Xin H., Hu H., Guo L., & Yang J. (**2025**). Deep learning-assisted piezoresistive pressure sensors with broad-range ultrasensitivity for wearable motion monitoring. *Nano Energy,* 140, 111035. doi: 10.1016/j.nanoen.2025.111035.

[25] Gu M., Zhou X., Shen J., Xie R., Su Y., Gao J., Zhao B., Li J., Duan Y., Wang Z., Hu Y., Gu G., Wang L., Wei L., Yang C., & Chen M. (**2024**). High-sensitivity, ultrawide linear range, antibacterial textile pressure sensor based on chitosan/MXene hierarchical architecture. *iScience,* 27(4), 109481. doi: 10.1016/j.isci.2024.109481.

[26] Shi Y., Lu X., Wang W., Meng X., Zhao J., Wang P., & Bai G. (**2021**). Multilayer Flexible Pressure Sensor With High Sensitivity Over Wide Linearity Detection Range (August 2021). *IEEE Transactions on Instrumentation and Measurement,* 70, 1-9. doi:10.1109/TIM.2021.3101307.

[27] Zhang Y., Lu Q., He J., Huo Z., Zhou R., Han X., Jia M., Pan C., Wang Z. L., & Zhai J. (**2023**). Localizing strain via micro-cage structure for stretchable pressure sensor arrays with ultralow spatial crosstalk. *Nature Communications,* 14(1), 1252. doi:10.1038/s41467-023-36885-3.

[28] Ma H., Si F., He C., Wang X., Ding J., Zhang W., & Fan X. (**2025**). Fully printed all-resistive dual-mode sensor with ultra-low temperature coefficient of resistance for crosstalk-free detections of pressure and humidity. *Chemical Engineering Journal,* 505, 159394. doi:10.1016/j.cej.2025.159394.

[29] Si Z., Yu T. C., Morozov K., McCann J., & Yuan W. (2023). RobotSweater: Scalable, Generalizable, and Customizable Machine-Knitted Tactile Skins for Robots. In 2023 IEEE International Conference on Robotics and Automation (ICRA), pp. 10352-10358. IEEE. doi: 10.1109/ICRA48891.2023.10161321.

[30] Cao L., Xiong Z., Huang J., Liu Z., Chen J., & Zhu Y. (**2025**). Hierarchical-engineered all-textile piezoresistive sensors balancing high sensitivity, wide linearity, and superior breathability for human motion sensing. *Chemical Engineering Journal*, 524, 169575. doi: 10.1016/j.cej.2025.169575.

[31] Ke Y., Jia K., Zhong W., Ming X., Jiang H., Chen J., Ding X., Li M., Lu Z., & Wang D. (**2022**). Wide-range sensitive all-textile piezoresistive sensors assembled with biomimetic core-shell yarn via facile embroidery integration. *Chemical Engineering Journal,* 435, 135003. doi: 10.1016/j.cej.2022.135003.

[32] Qiu S., Deng S., Pang H., & Wang B. (**2026**). A grid-structured textile pressure sensor for machine learning-assisted tactile sensing and intelligent driving safety. *Colloids and Surfaces A: Physicochemical and Engineering Aspects,* 746, 140770. doi:10.1016/j.colsurfa.2026.140770.

[33] Lu P., Wang L., Zhu P., Huang J., Wang Y., Bai N., Wang Y., Li G., Yang J., Xie K., Zhang J., Yu B., Dai Y., & Guo C. F. (**2021**). Iontronic pressure sensor with high sensitivity and linear response over a wide pressure range based on soft micropillared electrodes. *Science Bulletin,* 66(11), 1091-1100. doi:10.1016/j.scib.2021.02.019.

[34] Yang R., Dutta A., Li B., Tiwari N., Zhang W., Niu Z., Gao Y., Erdely D., Xin X., Li T., & Cheng H. (**2023**). Iontronic pressure sensor with high sensitivity over ultra-broad linear range enabled by laser-induced gradient micro-pyramids. *Nature Communications,* 14(1), 2907. doi: 10.1038/s41467-023-38274-2.

[35] Su Q., Zou Q., Li Y., Chen Y., Teng S.-Y., Kelleher J. T., Nith R., Cheng P., Li N., Liu W., Dai S., Liu Y., Mazursky A., Xu J., Jin L., Lopes P., & Wang S. (2021). *A stretchable and strain-unperturbed pressure sensor for motion interference-free tactile monitoring on skins. Science Advances,* 7(48), eabi4563. doi:10.1126/sciadv.abi4563.

[36] Yu H., Guo H., Wang J., Zhao T., Zou W., Zhou P., Xu Z., Zhang Y., Zheng J., Zhong Y., Wang X., & Liu L. (**2024**). Skin - Inspired Capacitive Flexible Tactile Sensor with an Asymmetric Structure for Detecting Directional Shear Forces. *Advanced Science,* 11(6), 2305883. doi: 10.1002/advs.202305883.

[37] Yin M., Guo Y., An J., Liu T., Gou G., Li T., Chen G., Ma T., Sun J., Han M., Cheng J., Zhou J., Sun X., Zhuang C., Li H., Liu C., Qi Z., & Xue N. (**2024**). Flexible wide-range, sensitive three-axis pressure sensor array for robotic grasping feedback. *Sensors and Actuators Reports,* 8, 100250. doi: 10.1016/j.snr.2024.100250.

[38] Ergun S., Mishra R. B., Ananadan N., Mitterer T., Mattoli V., & Zangl H. (**2026**). CapTac: Robust Capacitive Sensing for Distributed Force Mapping in Parallel Robotic Grasping. *IEEE Robotics and Automation Letters,* 11(3), 3668-3675. doi: 10.1109/lra.2026.3662613.

[39] Berman A., Shi B., Zaluska T., Yong A., Clees S., Xu C., Beker L., & Bao Z. (**2025**). A skin-inspired, capacitive array for tactile modulus detection via a scalable rigid-island architecture. *npj Flexible Electronics,* 10(1), 5. doi: 10.1038/s41528-025-00503-7.

[40] Lim H., Choi J., Han C., Kim D., Jin H., Kim M., Kim Y., Yang J., Seo S., Jung J., Ju H., Hong C.-H., Lee D., Ahn J., & Kim H. J. (**2026**). Scalable in-situ fabrication of multimodal electronic skin for intelligent robotics and interactive systems. *npj Flexible Electronics,* 10(1), 34. doi: 10.1038/s41528-026-00538-4.

[41] Chen Y., Cao J., Qiu J., Yang D., Liu M., Zhang M., Li C., Wu Z., Yu J., Zhang X., Chen X., Huang Z., Song E., Wang M., Liu Q., & Liu M. (**2025**). Capacitive in-sensor tactile computing. *Nature Communications,* 16(1), 5691. doi: 10.1038/s41467-025-60703-7.

[42] Pagoli A., Chapelle F., Corrales-Ramon J.-A., Mezouar Y., & Lapusta Y. (**2022**). Large-Area and Low-Cost Force/Tactile Capacitive Sensor for Soft Robotic Applications. *Sensors,* 22 (11), 4083. doi:10.3390/s22114083.

[43] An B. W., Heo S., Ji S., Bien F., & Park J. -U. (**2018**). Transparent and flexible fingerprint sensor array with multiplexed detection of tactile pressure and skin temperature. *Nature Communications,* 9(1), 2458. doi:10.1038/s41467-018-04906-1.

[44] Liu Y., Wang J., Liu T., Wei Z., Luo B., Chi M., Zhang S., Cai C., Gao C., Zhao T., Wang S., & Nie S. (**2025**). Triboelectric tactile sensor for pressure and temperature sensing in high-temperature applications. *Nature Communications,* 16(1), 383. doi:10.1038/s41467-024-55771-0.

[45] Xian S., Wu Z., Li Y., Wu Z., & Zhong Y. (**2024**). All-in-one, flexible, diversified self-powered sensors through embedded 3D printing. *Smart Materials and Structures,* 33(12), 125040. doi:10.1088/1361-665X/ad939b.

[46] Xian S., Xu Y., Li Y., Wu Z., Xie X., Wu Z., Yang X., & Zhong Y. (**2025**). Flexible Triboelectric Sensor based on Catalyst - Diffusion Self - Encapsulated Conductive Liquid - Metal - Silicone Ink for Somatosensory Soft Robotic System. *Advanced Functional Materials*, 35(2), 2412293. doi:10.1002/adfm.202412293.

[47] Ahbab N., Naz S., Xu T. -B., & Zhang S. (**2025**). A Comprehensive Review of Piezoelectric PVDF Polymer Fabrications and Characteristics. *Micromachines,* 16(4), 386. doi:10.3390/mi16040386.

[48] Alotaibi A., & Anwar S. (**2021**). Direct and Extended Piezoresistive and Piezoelectric Strain Fusion for a Wide Band PVDF/MWCNT-Based 3D Force Sensor. *IEEE Access,* 9, 162156-162174. doi:10.1109/ACCESS.2021.3129319.

[49] Ha X. T., Wu D., Ourak M., Borghesan G., Dankelman J., Menciassi A., & Poorten E. V. (**2023**). Shape Sensing of Flexible Robots Based on Deep Learning. *IEEE Transactions on Robotics,* 39(2), 1580-1593. doi: 10.1109/tro.2022.3221368.

[50] Mo L., Li Y., Fu S., Xia J., Zhang Y.-F., Zhong Y., Chen X., & Chase J. G. (**2026**). A Highly Sensitive, Compact, and Low-Cost Soft Triaxial Optical Force (STOF) Sensor for Robotic Grasping and Human-Machine Interaction. *IEEE Transactions on Industrial Electronics,* 73(1), 1469-1480. doi: 10.1109/TIE.2025.3603085.

[51] Yang Y., Zhou X., Yang R., Zhang Q., Sun J., Li G., Zhao Y., & Liu Z. (**2024**). Real-Time 3-D Force Measurements Using Vision-Based Flexible Force Sensor. *IEEE Transactions on Instrumentation and Measurement,* 73, 1-10. doi: 10.1109/TIM.2023.3335510.

[52] Qu X., Ma F., Zhao S., Yang L., Wu Z., & Chen B. (**2025**). Analysis of the Influence of Macro-Bending Loss in Single-Mode Optical Fibers on OFDR Signal Quality. *Sensors,* 25 (22), 6983. doi:10.3390/s25226983.

[53] Fang Y., Dong X., Mohammad A., & Axinte D. (**2023**). Design and Control of a Multiple-Section Continuum Robot With a Hybrid Sensing System. *IEEE/ASME Transactions on Mechatronics*, 28(3), 1522-1533. doi:10.1109/tmech.2022.3229188.

[54] Lu G., Ni E., Jiang Y., Wu W., & Li H. (**2024**). Room - Temperature Liquid Metals for Flexible Electronic Devices. *Small,* 20(9), 2304147. doi:10.1002/smll.202304147.

[55] Ma J., Krisnadi F., Vong M. H., Kong M., Awartani O. M., & Dickey M. D. (**2023**). Shaping a Soft Future: Patterning Liquid Metals. *Advanced Materials,* 35(19), 2205196. doi: 10.1002/adma.202205196.

[56] Chen H., Furfaro I., Fernández Lavado E., & Lacour S. P. (**2024**). Liquid Metal - Based Sensor Skin Enabling Haptic Perception of Softness. *Advanced Functional Materials,* 34 (31), 2308698. doi:10.1002/adfm.202308698.

[57] Xu J., Guo H., Ding H., Wang Q., Tang Z., Li Z., & Sun G. (**2021**). Printable and Recyclable Conductive Ink Based on a Liquid Metal with Excellent Surface Wettability for Flexible Electronics. *ACS Applied Materials & Interfaces,* 13(6), 7443-7452. doi:10.1021/acsami.0c20549.

[58] Rahim Md. A., Centurion F., Han J., Abbasi R., Mayyas M., Sun J., Christoe M. J., Esrafilzadeh D., Allioux F. -M., Ghasemian M. B., Yang J., Tang J., Daeneke T., Mettu S., Zhang J., Uddin M. H., Jalili R., & Kalantar-Zadeh K. (2021). *Polyphenol-Induced Adhesive Liquid Metal Inks for Substrate-Independent Direct Pen Writing. Advanced Functional Materials,* 31(10), 2007336. doi:10.1002/adfm.202007336.

[59] Zhou Z., Zuo R., Ying B., Zhu J., Wang Y., Wang X., & Liu X. (**2024**). A Sensory Soft Robotic Gripper Capable of Learning-Based Object Recognition and Force-Controlled Grasping. *IEEE Transactions on Automation Science and Engineering,* 21(1), 844-854. doi:10.1109/tase.2022.3228255.

[60] Dai X., Wu Y., Liang Q., Yang J., Huang L. -B., Kong J., & Hao J. (**2023**). Soft Robotic - Adapted Multimodal Sensors Derived from Entirely Intrinsic Self - Healing and Stretchable Cross - Linked Networks. *Advanced Functional Materials,* 33 (44), 2304415. doi:10.1002/adfm.202304415.

[61] Chen Y., Wu Z., & Zhong Y. (2022). Design and Fabrication of a Sensorized Soft Actuator via Embedded 3D Printing. In 2022 5th International Conference on Intelligent Robotics and Control Engineering (IRCE), pp. 82-87. IEEE. doi: 10.1109/IRCE55557.2022.9963081.

[62] Kohlbrenner C., Soukhovei A., Escobedo C., Nechyporenko N., & Roncone A. (**2026**). Design, Mapping, and Contact Anticipation with 3D-printed Whole-Body Tactile and Proximity Sensors. arXiv preprint arXiv: 2603.*04714* . doi: 10.48550/arXiv.2603.04714.

[63] Yang M. J., Chung H., Kim Y., Park K., & Kim J. (**2025**). A Body-Scale Robotic Skin Using Distributed Multimodal Sensing Modules: Design, Evaluation, and Application. *IEEE Transactions on Robotics,* 41, 96-109. doi: 10.1109/TRO.2024.3502204.

[64] Shih B., Shah D., Li J., Thuruthel T. G., Park Y. -L., Iida F., Bao Z., Kramer-Bottiglio R., & Tolley M. T. (**2020**). Electronic skins and machine learning for intelligent soft robots. *Science Robotics,* 5(41), eaaz9239. doi: 10.1126/scirobotics.aaz9239.

[65] Johnson C. C., Webb D., Hill D., & Killpack M. D. (**2025**). Scaling Fabric-Based Piezoresistive Sensor Arrays for Whole-Body Tactile Sensing. *arXiv preprint arXiv* :2508.20959. doi: 10.48550/arXiv.2508.20959.

[66] Chefchaouni Moussaoui S., Cisneros-Limón R., Kaminaga H., Benallegue M., Nobeshima T., Kanazawa S., & Kanehiro F. (**2023**). Spatial Calibration of Humanoid Robot Flexible Tactile Skin for Human-Robot Interaction. *Sensors,* 23(9), 4569. doi:10.3390/s23094569.

[67] Jiao R., Wang R., Wang Y., Cheung Y. K., Chen X., Wang X., Deng Y., & Yu H. (**2023**). Vertical serpentine interconnect-enabled stretchable and curved electronics. *Microsystems & Nanoengineering,* 9(1), 149. doi: 10.1038/s41378-023-00625-w.

[68] Ham J., Han A. K., Cutkosky M. R., & Bao Z. (**2022**). UV-laser-machined stretchable multi-modal sensor network for soft robot interaction. *npj Flexible Electronics,* 6(1), 94. doi: 10.1038/s41528-022-00225-0.

[69] Liu Y., Yiu C., Song Z., Huang Y., Yao K., Wong T., Zhou J., Zhao L., Huang X., Nejad S. K., Wu M., Li D., He J., Guo X., Yu J., Feng X., Xie Z., & Yu X. (**2022**). Electronic skin as wireless human-machine interfaces for robotic VR. *Science Advances,* 8(2), eabl6700. doi:10.1126/sciadv.abl6700.

[70] Pang G., Yang G., & Pang Z. (**2021**). Review of Robot Skin: A Potential Enabler for Safe Collaboration, Immersive Teleoperation, and Affective Interaction of Future Collaborative Robots. *IEEE Transactions on Medical Robotics and Bionics,* 3(3), 681-700. doi: 10.1109/tmrb.2021.3097252.

[71] Vo N. T. P., Nam T. U., Jeong M. W., Kim J. S., Jung K. H., Lee Y., Ma G., Gu X., Tok J. B.-H., Lee T. I., Bao Z., & Oh J. Y. (**2024**). Autonomous self-healing supramolecular polymer transistors for skin electronics. *Nature Communications,* 15 (1), 3433. doi:10.1038/s41467-024-47718-2.

[72] Zhang Y., Yuan Y., Yu H., Cai C., Sun J., & Tian X. (**2024**). A stretchable conductive elastomer sensor with self-healing and highly linear strain for human movement detection and pressure response. *Materials Horizons,* 11(16), 3911-3920. doi:10.1039/d4mh00448e.

[73] Wang C., Duan X., Li X., Pan W., Ning C., Wang F., Cao W., Ou F., Wang M., Liang Q., Gao W., Li Z., & Zhao S. (**2024**). A Self - Healing Solid - State Ion - Conductive Elastomer with High Mechanical Robustness and High Conductivity for Soft Ionotronics. *Advanced Functional Materials,* 34(38), 2402815. doi:10.1002/adfm.202402815.

[74] Li Y., Geng J., Ye M., He J., Zheng X., Wang Q., & Zhao Y. (**2024**). A CMOS Readout Circuit for Resistive Tactile Sensor Array Using Crosstalk Suppression and Nonuniformity Compensation Techniques. *IEEE Transactions on Very Large*

Scale Integration (VLSI) Systems, 32(12), 2368-2376. doi: 10.1109/TVLSI.2024.3447164.

[75] Abdul-Hussain G., Holderbaum W., Theodoridis T., & Wei G. (**2023**). Modified Nonlinear Hysteresis Approach for a Tactile Sensor. *Sensors,* 23(16), 7293. doi:10.3390/s23167293.

[76] Li S., Chen X., Li X., Tian H., Wang C., Nie B., He J., & Shao J. (**2022**). Bioinspired robot skin with mechanically gated electron channels for sliding tactile perception. *Science Advances,* 8(48), eade0720. doi:10.1126/sciadv.ade0720.

[77] Li H., Dikhale S., Cui J., Iba S., & Jamali N. (2024). HyperTaxel: Hyper-Resolution for Taxel-Based Tactile Signals Through Contrastive Learning. In 2024 IEEE/RSJ International Conference on Intelligent Robots and Systems (IROS), pp. 7499-7506. IEEE. doi: 10.1109/IROS58592.2024.10802001.

[78] Patel N., Rana R., Kumar D., & Thakor N. V. (**2025**). SuperTac - tactile data super-resolution via dimensionality reduction. *Frontiers in Robotics and AI,* 12, 1552922. doi: 10.3389/frobt.2025.1552922.

[79] Husák M., Mihálik O., Dvorský P., & Bradáč Z. (**2024**). A Method of Tactile Resistive Sensor Array Calibration. *IFAC-PapersOnLine,* 58(9), 37-42. doi:10.1016/j.ifacol.2024.07.368.

[80] Gao J., Zhu X., Fu Z., Zhang W., Sun D., & Gu W. (**2024**). A Grid-Less Flexible Tactile Sensing System Based on Deep Neural Network for Two-Point Localization and Shape Recognition. *IEEE Sensors Journal,* 24(11), 18259-18266. doi:10.1109/JSEN.2024.3387067.

[81] Kong D., Lu Y., Zhou S., Wang M., Pang G., Wang B., Chen L., Huang X., Lyu H., Xu K., & Yang G. (**2025**). Super-resolution tactile sensor arrays with sparse units enabled by deep learning. *Science Advances,* 11(27), eadv2124. doi: 10.1126/sciadv.adv2124.

[82] Lu Y., Kong D., Yang G., Wang R., Pang G., Luo H., Yang H., & Xu K. (**2023**). Machine Learning - Enabled Tactile Sensor Design for Dynamic Touch Decoding. *Advanced Science,* 10 (32), 2303949. doi:10.1002/advs.202303949.

[83] Ding Z., Chen G., Wang Z., & Sun L. (**2023**). Adaptive visual-tactile fusion recognition for robotic operation of multi-material system. *Frontiers in Neurorobotics,* 17, 1181383. doi: 10.3389/fnbot.2023.1181383.

[84] Mandil W., & Ghalamzan-E A. (**2026**). Multi-modal world model for physical robot interactions: Simultaneous visual and tactile predictions for enhanced accuracy (SPOTS). *Robotics and Autonomous Systems,* 204, 105512. doi:10.1016/j.robot.2026.105512.

[85] Li Y., Chen Y., Zhao Z., Li P., Liu T., Huang S., & Zhu Y. (**2026**). Simultaneous Tactile-Visual Perception for Learning Multimodal Robot Manipulation. *IEEE Robotics and Automation Letters*, 11(4), 5254-5261. doi: 10.1109/LRA.2026.3671701.

[86] Cao Z., Tian D., Guan R., Mu Y., Sun X., Liang S., Liu D., Huang T., Yue Y., Ding H., Fang B., Zhou A., Han Q.-L., & Xiong H. (**2026**). Tactile-based Multimodal Fusion in Embodied Intelligence: A Survey of Vision, Language, and Contact-Driven Paradigms. *arXiv preprint arXiv* :2605.17336. doi:10.48550/arXiv.2605.17336.

[87] Sekine T., Wang Y. -F., Hong J., Takeda Y., Miura R., Watanabe Y., Abe M., Mori Y., Wang Z., Kumaki D., Santos F. D. D., *Miyabo A.,* Kawamura S., & Tokito S. (**2021**). Artificial Cutaneous Sensing of Object Slippage using Soft Robotics with Closed-Loop Feedback Process. Small Science, 1(3), 2100002. doi:10.1002/smsc.202100002.

[88] Low J. H., Khin P. M., Han Q. Q., Yao H., Teoh Y. S., Zeng Y., Li S., Liu J., Liu Z., Valdivia y Alvarado P., Chen I.-M., *Tee B*. C. K., & Yeow C. H. (2022). Sensorized Reconfigurable Soft Robotic Gripper System for Automated Food Handling. IEEE/ASME Transactions on Mechatronics, 27(5), 3232-3243. doi:10.1109/tmech.2021.3110277.

[89] Min J., Ma J., Kwon J., Bae S., Kim J., & Park K. (**2026**). Tactile-Proprioceptive Sensor Fusion for Contact Wrench Estimation in Whole-Body Physical Human-Robot Interaction. arXiv preprint arXiv: 2605.*28412* . doi: 10.48550/arXiv.2605.28412.

[90] Sahu S. K., Tamadon I., Rosa B., Renaud P., & Menciassi A. (**2022**). A Spring-Based Inductive Sensor for Soft and Flexible Robots. *IEEE Sensors Journal,* 22(20), 19931-19940. doi:10.1109/jsen.2022.3201049.

[91] Lu Y., Chen W., Lu B., Zhou J., Chen Z., Dou Q., & Liu Y.-H. (**2024**). Adaptive Online Learning and Robust 3-D Shape Servoing of Continuum and Soft Robots in Unstructured Environments. *Soft Robotics,* 11(2), 320-337. doi: 10.1089/soro.2022.0158.

[92] Fan X., Lee D., Jackel L., Howard R., Lee D., & Isler V. (**2022**). Enabling Low-Cost Full Surface Tactile Skin for Human Robot Interaction. *IEEE Robotics and Automation Letters,* 7(2), 1800-1807. doi:10.1109/LRA.2022.3142433.

[93] Rustler L., Misar M., & Hoffmann M. (2024). Adaptive Electronic Skin Sensitivity for Safe Human-Robot Interaction. In 2024 IEEE-RAS 23rd International Conference on Humanoid Robots (Humanoids), pp. 475-482. IEEE. *doi: 10.1109/humanoids58906.2024.10769602*.

[94] Lin C., Zhang H., Xu J., Wu L., & Xu H. (**2024**). 9DTact: A Compact Vision-Based Tactile Sensor for Accurate 3D Shape Reconstruction and Generalizable 6D Force Estimation. *IEEE Robotics and Automation Letters,* 9(2), 923-930. doi:10.1109/LRA.2023.3339397.

[95] Liu J., Zeng T., Mohammad A., Axinte D., & Dong X. (**2026**). Design and Validation of a Fuzzy Logic Controller for Multisection Continuum Robots. *IEEE Transactions on Industrial Electronics*, 73(3), 4460-4471. doi: 10.1109/TIE.2025.3626667.

[96] Wild S., Elsayed B. A., Shi H., Jones S. D., Zeng T., Mohammad A., Axinte D., & Dong X. (**2026**). Unified Neural Network-Based Shape Sensing for Continuum Robots Using Fiber Bragg Gratings. *IEEE Sensors Journal,* 26(1), 399-406. doi:10.1109/JSEN.2025.3626890.

[97] Ferguson J. M., Rucker D. C., & Webster R. J. (**2024**). Unified Shape and External Load State Estimation for Continuum Robots. *IEEE Transactions on Robotics,* 40, 1813-1827. doi:10.1109/tro.2024.3360950.